TR-PIV FLOW CHARACTERIZATION OF BLOCKAGE EFFECTS ON A 61-PIN WIRE-WRAPPED HEXAGONAL FUEL BUNDLE

A Thesis

by

LANCE LEON ALLEN WHITE

Submitted to the Office of Graduate and Professional Studies of
Texas A&M University
in partial fulfillment of the requirements for the degree of

MASTER OF SCIENCE

Chair of Committee,	Yassin A. Hassan
Committee Members,	Rodolfo Vaghetto
	Victor M. Ugaz
Head of Department,	Michael Nastasi

December 2019

Major Subject: Nuclear Engineering

Copyright 2019 Lance Leon Allen White

ABSTRACT

Liquid metal fast reactors often use a tightly packed triangular lattice of fuel pins that are helically wrapped with a wire spacer, enclosed in a hexagonal duct. These reactors are thought to suffer from partial or total flow blockage of coolant in various subchannel locations throughout the fuel assembly. These blockages can result from a large range of causes including debris accumulation and cladding deformation, or the combination of the two. Flow in these reactor fuel assemblies are complex, and the addition of a blockage increases that complexity as well. The effect of blockages on flow behavior in liquid metal fast breeder reactors is relatively unknown, especially experimentally, with only one recent study exploring the subject. This absence of information has motivated researchers globally to begin investigations to explore the effects of blockages on these geometries.

The matched index of refraction 61-pin wire-wrapped experimental fuel bundle at Texas A&M, with the optically clear and accessible test section was designed with the express purpose of exploring flow behavior for this geometry of fuel assemblies. The experiments carried out on this facility are high-fidelity velocity and pressure measurements. High spatial and temporal-resolution particle image velocimetry measurements were conducted in this experiment to explore the flow behavior and effects of two blockage cases in a wire-wrapped bundle.

Time-resolved particle image velocimetry measurements were conducted at two vertical planes in the facility, Center 2 and Exterior 1. Two blockage types were also

explored, a single subchannel at Center 2, and a larger edge subchannel blockage at Exterior 1. Instantaneous velocity fields obtained from these measurements lead to the production of first and second order flow statistics such as the mean velocity, root-mean-square fluctuating velocity, and Reynolds shear stress. These experimental results provide a greater understanding of the flow behavior of a subchannel under a blockage scenario, while providing data available for validation of advanced CFD simulations using RANS or LES with unique experimental data sets. As this work continues more blockages geometries are expected to be explored, paired with friction factor experiments to examine the effect of a blockage on those parameters.

DEDICATION

This work is dedicated to Rosalinda Ramirez, Linda Jo Cabral, Pantaleon and Eufelia Salas, Richard Millette, and Richard Roberts. Those that I know would have loved to see this achievement.

ACKNOWLEDGEMENTS

I would like to thank my committee chair, Dr. Hassan, and my committee members Dr. Vaghetto, and Dr. Ugaz, along with the immense assistance from Dr. Nguyen for their guidance and support throughout the course of this research.

I would also like to thank Dr. Nolan Goth, Phillip Jones, Dr. Mason Childs, Dr. Se Ro Yang, Ethan Kappes, Robert Muyshondt William Headley, Blazedale Boyer, Jadyn Reis, Collin Guilbault, and Jake Pettyjohn for all their help in this research.

Finally, thanks to my wife Robyn Lynn Smith White who has been with me on this journey from the very beginning, to my parents Dennis and Charlene White, who from a young age pushed me achieve in everything that I do and have supported me my whole life through everything, to all of my mentors over the years who have challenged me and helped me grow into the academic I am today, and to the entire Thermal-Hydraulics lab and the great friends I've made here in my time at TAMU.

CONTRIBUTORS AND FUNDING SOURCES

Contributors

This work was supervised by a thesis committee consisting of Dr. Yassin Hassan and Dr. Rodolfo Vaghetto of the Department of Nuclear Engineering and Dr. Victor Ugaz of the Department of Chemical Engineering.

Funding Sources

Graduate study was supported by Pathways to a Doctorate Fellowship from Texas A&M University and Graduate Research and Teaching Assistantships from the department of Nuclear Engineering at Texas A&M University.

This work was made possible by the U.S. Department of Energy (DOE), Nuclear Energy University Program (NEUP) under a contract DE-NE000832. Its contents are solely the responsibility of myself, the author, and do not necessarily represent the official views of the DOE.

TABLE OF CONTENTS

Page

LIST OF FIGURES

Page

LIST OF TABLES

Page

1. INTRODUCTION

Fast spectrum reactors have been an area of interest in the field of nuclear engineering for over 60 years. This interest was driven by the comparatively high resource efficiency of a fast spectrum breeder reactor and a seemingly limited uranium reserve estimate expected to be depleted by 2020. The efficiency of a fast spectrum breeder reactor lead to this reactor type being considered a possible solution to the uranium supply issue. The Atomic Energy Commission (AEC) steered reactor research to focus on liquid metal fast breeder reactors (LMFBR) rather than other thermal and fast breeding systems in 1967. Specifically, the sodium fast reactor (SFR) LMFBR was the design investigated the longest during this time when the breeder reactors initially were researched. Between the late ‘70s and early ‘90s the United States uranium reserves expanded, and a general decline in demand for nuclear power was experienced which lead to the end of the Integral Fast Reactor program essentially leaving the SFR development in a stasis until relatively recent efforts to again explore the potential of a LMFBR SFR reactor.

An LMFBR fuel assembly usually consists of triangular lattice arranged fuel rods in a hexagonal duct. Each rod is wrapped helically with a stainless-steel wire spacer. This geometric complexity and difference from other fuel types leads to difficulty when looking at analytical solutions for thermal-hydraulic analysis of a core with this fuel type. This lack of analytical solvability results in the need of computational fluid dynamics (CFD) as a tool for empirical analysis of the coolant flow behavior. Analysts

using CFD are employing Reynolds Averaged Navier Stokes (RANS) and large eddy simulation (LES) to liquid metal fast reactor assemblies with the purpose of reducing the conservatisms that currently exist in thermal-hydraulic analysis codes when considering liquid metal as a coolant. Thermal-hydraulic behavior in the past was examined through experiments; however, the collected data was not of a high enough temporal or spatial resolution to be of use by CFD analysts working with RANS or LES validation for flow behavior at exterior, corner, or edge subchannels. This is due to the invasive measurement techniques used such as intrusive thermocouple probes.

LMFBR fuel assembly experimental flow loops that have used particle image velocimetry (PIV) and laser Doppler velocimetry (LDV) in the past and attempted to quantify flow behavior utilizing these measurement techniques. Those experiments suffered from a low rod count of 7 and 19 which Brockmeyer [1] found to be too few to neglect the effects of the hexagonal wall. A demand for finer spatial and temporal resolution PIV and LDV data has begun to increase with the advent of more powerful computing and the desire to more closely examine the behavior of larger bundles which are believed to behave closer to the industry standard 217-rod assemblies.

The U.S. Department of Energy funded a joint project in order to generate CFD validation data for reference with the final objective of extending the lifetime of hexagonal fuel assemblies. The team members of the project included FRAMATOME (previously AREVA), Argonne National Lab (ANL), TerraPower, and Texas A&M University (TAMU). In this team FRAMATOME gathered temperature and pressure measurements on a 61-rod heated assembly [2] [3] and TAMU performed velocity and

pressure measurements on a 61-rod isothermal assembly. Each facility had very similar pitch-to-diameter ratios (P/D) in the effort to achieve similar flow behavior. ANL and TerraPower performed LES and RANS simulations on both the FRAMATOME and TAMU experimental assembly geometries.

The initial research conducted at Texas A&M University by Nolan Goth and Phillip Jones began to satisfy that demand by focusing on several components. The first was a literature review, then material testing, designing, and building a facility to study a 61-pin wire-wrapped bundle under isothermal and under steady state flow. The second objective was to shakedown the facility and calibrate\install the instrumentation utilized by using first water to eliminate leaks and vibration, then later the working matched index of refraction (MIR) fluid para-cymene (p-cymene). Finally, the last objective was to operate at those isothermal and steady state conditions and collect TR-PIV and pressure measurements for an unblocked wire-wrapped bundle and create a database of information. These efforts of collecting the time resolved particle image velocimetry (TR-PIV) measurements and pressure measurements throughout the facility have been completed, resulting in flow field calculations and friction factor calculations completed and disseminated from this first phase of research through journal articles and conference proceedings.

This thesis work begins at the second phase of this project where the main funding source shifted from a joint team project to a grant supplied by the Nuclear Engineering University Project (NEUP) funding opportunity awarded in October of 2017 under the project number DE-NE0008652. This project has since been broken up

into three major sections. The first being exploring the different options to complete a novel concept for a top down imaging technique completed by Nolan Goth for his PhD dissertation work and disseminated in the 2018 ANS Winter and 2018 ICONE conferences. The next phase of this project is the basis of this thesis, the implementation of subchannel blockage geometries and analysis of flow behavior induced by those blockages by the usage of TR-PIV measurement techniques. This current phase is also still in progress as there is pressure data being examined and new blockage geometries being considered for the next steps in the project. The next phase will include more blockage investigation and possibly a heated bundle component.

This thesis provides the information on the approach and conditions that were used to implement a core blockage into the current existing 61-pin wire-wrapped facility at Texas A&M University and the collection and methodology used for acquisition of data on those core blockages.

2. OBJECTIVES

The primary objective of this research is to examine the effects of subchannel blockages inside of a wire-wrapped fuel bundle and provide the resulting data to further the application of CFD codes in nuclear safety and modeling issues when various blockage scenarios are considered that could occur during operation of a LMBFR with a wire-wrapped fuel type. The blockage effects will be examined through the collection, processing and analysis of PIV data.

As of yet there is no other experimental data available, aside from what has been collected under the work of this project, on the effects of a blockage in a wire-wrapped 61-pin fuel bundle, specifically flow field data collected through a MIR TR-PIV measurement technique.

3. LITERATURE REVIEW

A literature review was performed here to explore the available literature for flow behavior of a 61-pin wire wrapped fuel assembly both without and with a blockage, along with MIR experiments and their success and shortfalls. This review covers what has been previously covered when this project began and bleeds into the current available literature.

3.1. Last Century Research

Liquid metal fast reactors that use sodium as a coolant typically contain a tightly packed triangular lattice fuel pin geometry enclosed within a hexagonal duct. The fuel pins are often wrapped helically with a stainless steel wire that acts as a spacer maintaining the gap between the fuel pins along with mitigating vortex-induced vibrations and enhancing subchannel mixing with the ultimate goal of increasing convective heat transfer [4].

LMFBRs are very dependent on the cooling capability of the liquid metal working fluid to transfer heat away from the fuel operation. Blockages within the core prevent the flow of liquid metal coolant and subsequentially the reactor fuel rods and surrounding materials develop hotspots where flow is reduced. Saxena found using large eddy simulations that hot spots and a cyclical temperature variation can appear and adversely affect the cladding properties due to thermal stripping [5]. Although, Pointer has shown that helical wires in these bundles inherently induce traversal flow, thus enhancing the heat transfer [6]. Both authors agree that the wire does create a wake

behind it and that the wire does increase pressure drop and turbulence in the assembly. The contributions of helical wires in a fuel assembly are contested, therefore numerical and experimental investigations of the flow in the wire-wrapped fuel assembly are essential.

The first experiment presenting coolant mixing results in a full-scale model of a wire-wrapped LMFBR was performed by Collingham where the facility was a 217-pin fuel bundle [7]. The facility was monitored with over 400 probes and the resulting data were proposed as two models for turbulent mixing and cross flow within the bundle. In 1977 Lorenz and Ginberg addressed that prior work had been focused on interior subchannel characterization and decided to base their work on the characterization of edge subchannels [8]. Electrolytic tracers and isokinetic sampling techniques were used on a 91-pin assembly, and those same techniques were also applied to the measurements taken by Collingham to reduce the uncertainty of those measurements. Experiments examining pressure drop have been conducted extensively to study the thermal-hydraulic characteristics of these wire-wrapped fuel assemblies.

In 1972 Novendstern developed a semi-empirical model predicting pressure loss in a hexagonal wire-wrapped array of fuel pins in the turbulent flow regime [9]. In 1973 Rheme proposed pressure drop correlations for an expansive range of geometric parameters, such as P/D between 1.125 and 1.417, lead-to-wire diameter ratio between 6 and 45, and a pin count from 7 to 61 [10]. Cheng and Todreas released their hydrodynamic models for subchannel friction factors and mixing parameters in a 37-pin fuel bundle, covering the laminar, transition, and turbulent flow regimes [11].

3.2. Twenty-First Century Developments

3.2.1. Computational Techniques and Methods

As computational capabilities have increased over time, CFD has become an increasingly opportune method to validate these older correlations, along with investigating the phenomena in these subchannels at a scale previously inconceivable. Numerical studies of the wire-wrapped fuel assembly have been performed, mostly Reynolds Averaged Navier-Stokes (RANS) simulations with an assortment of turbulence models. Ahmad and Kim completed RANS simulations of 7 and 19-pin bundles using the k-ω SST turbulent model, and Rolfo examined the heat transfer in 7, 19, and 61-pin bundles also using RANS [12] [13]. Utilizing RANS and the k-ε model, Gajapathy examined the behavior of a 7-pin fuel bundle as well [14]. Mezari discusses a benchmark of RANS calculations for a 7-pin fuel bundle conducted among several groups and examined the differences between those findings [15].

RANS calculations using k-ε and k-ω turbulence models for 37-pin fuel bundles have recently been presented by Rasu and Jeong [16] [17]. Fischer has performed LES calculations on a wire-wrapped fuel bundle to collect higher-resolution numerical subchannel behavior data for transient behavior in those subchannels [4]. Brockmeyer has conducted a study on the dependency of the inter-subchannel flow exchange on a wire-wrapped fuel assembly's size utilizing RANS CFD. Brockmeyer focused on 19-, 37-, 61-, and 91-rod assemblies, concluding that the a minimum of a 37-rod assembly would be necessary to mitigate the effects from the wall, but a 61- or 91-rod assembly would be closer to an ideal scenario for an experiment [1].

3.2.2. Experimental Optical Techniques

Optical techniques of visualizing flow have been increasingly popularized with the advent of advances in charge-coupled device (CCD) cameras, computational performance, and non-intrusiveness inherent of the technique. Laser Doppler Velocimetry (LDV) was one of the first visualization techniques to gain momentum. LDV uses photon fringe interference patterns to be able to quantify a velocity vector around a single point in a very small volume. PIV was the next technique to surface and is able to produce vector fields that are in two and three dimensions depending on the specifics of the camera setup. The increased interest in LMFBRs and the inherent difficulty of measuring the internal phenomena within these bundles has led to applications of these non-intrusive visualization techniques on scaled facilities with the intention to reach similar flow conditions and then measure the behavior in these scaled facilities.

Idaho National Lab INL designed a 7-rod wire-wrapped hexagonal fuel assembly in 2008 with the intention of being the first experiment capable of measuring and recording velocity fields for interior subchannels of a LMFBR assembly [18]. The matched index materials that INL chose were a well-known and tested combination of mineral oil and quartz tubes and rods. This choice of materials began the limitations of the performance of the facility. The higher viscosity of mineral oil meant that the pump required to reach higher Reynolds numbers (Re #) would also generate heat in the facility. The target Re # for INL was 22,000, so the assembly size was chosen to be a 7-pin facility in order to achieve those higher Re # and still be able to pump and reject heat

at a rate that kept the materials well within matched index. This facility ended up with very large rods and wires with diameters of 85 mm and 25 mm respectively. The rods were made of quartz tubes, and wires of quarts rods. The inlet ends of the tubes were sealed and the rods were heated to a softening point and the wrapped around the tubes and attached at the ends similar to how a typical wire wrapped fuel rod is manufactured in practice. Additionally, Nishimura conducted PIV measurements on a small 3-rod bundle to attempt to quantify the interior subchannel behavior [19]. Sato used PIV and LDV both to examine the interior subchannel flow around a central rod within a 7-rod bundle while also investigating the impact of a deformed bundle where the central rod was subject to a bowing deformation [20].

3.2.2.1. MIR Facilities

Visualization of flow within these wire-wrapped fuel assemblies requires the materials to fall into the category of MIR materials. MIR facilities are applied in a larger range than only the wire-wrapped assembly geometry. A few of these facilities only at TAMU are the pebble bed, Westinghouse 5 x 5 assembly, and helical coil steam generator MIR experimental facilities.

Dominguez and Hassan constructed and developed an experimental MIR facility in 2009 to examine the flow behavior in a 5 x 5 rod bundle, a prototypical geometry for a Westinghouse pressurized water reactor (PWR) [21]. The pairing of materials for this facility was water as a working fluid and fluorinated ethylene propylene (FEP) for the rods. The index for these materials was at 1.33 for each at room temperature. This facility was constructed where the majority of the rod length was comprised of not FEP,

but polycarbonate until the visualization area, where the FEP tubes can be found and spacer grids are installed to observe the flow behavior around those grids.

A pebble bed facility headed by Nguyen also was also designed as a MIR facility. The materials chosen here were picked out of a review by Hassan and Dominguez where three material pairings were explored, FEP with water (1.33), PMMA with p-cymene or 60% volume aqueous sodium iodide (1.4873 and 1.49) [22]. While each of these parings are MIR, they optical clarity of the materials rely on more than just the index matching, but the homogeneity of the materials among other variables. This led to the choice of PMMA and p-cymene as the manufacturing process of PMMA can be well controlled, and the quality of p-cymene from suppliers is very pure and accessible [23].

The largest MIR facility in the world is the aforementioned facility housed at INL at the size of 0.6 m x 0.6 m x 2.5m. That facility uses the pairing of quartz and Drakeol 5 light mineral oil. The facilities size was determined for not only the current usage, but as a flexible size capable of future assemblies of various geometries, so long as they would fit inside of the facility. This versatility allows the facility to exist as a long-term solution for matched index experiments without massive overhauls for the facility to accommodate the new experiment specifications. This MIR facility also is equipped with a secondary loop where the temperature of the working fluid is controlled with a 20-ton glycol chiller and 8.5 kW heater, depending on the necessary conditions. This loop provides the capability of altering the fluid temperature at the inlet at a very fine control of ±0.05 °C. The measurement techniques used on this facility are PIV and

LDV and the equipment used to collect that data is focused on double exposure cameras and double pulsed neodymium-doped yttrium aluminum garnet lasers with optics that allow for laser sheets to be cast at 1 to 3 mm in thickness. That measurement hardware is mounted around the facility on three-dimensional traverse systems allowing for a wide range of measurements to be possible. Some difficulties with this facility are the inherent cost for quartz and large volumes of mineral oil, the leakage that can occur with mineral oil and the various seals around the facility, and lastly, as discussed before, the large amount of pumping power required to reach target Re #s that would be considered turbulent and representative of most operating flow conditions.

3.2.2.2. TAMU 61-Pin Wire-Wrapped Fuel Assembly

The facility constructed under the first round of research and funding by the DOE and partnerships with TerraPower, ANL, and FRAMATOME (AREVA) took many considerations from past MIR experiments and applied those to what exists now. The search for a suitable MIR compatible material pair began with the consideration of water and fluorinated resins. Casting the rods and wires out of a fluorinated resin Mexflon-DC™, used in Japan, was considered [19] [20]. However, discontinuation of the once commercially available resin made it unfeasible. FEP tubes similar to the ones used by Dominguez and Hassan were also considered, but the high flow rates expected for the facility brought up concerns of vibration in the bundle, and fabrication of the helically wrapped wires was determined to be unfeasible. Other fluoropolymers do exist; however, they do not possess a shear modulus that would be capable of withstanding the 2 m spans required for this facility.

A past experiment at TAMU considered the application of quartz and Drakeol 5 light mineral oil, but the prohibitive cost of using quarts for the solid components of any test section, along with the high viscosity of the fluid required significantly more equipment to reach desirable turbulent Re # and maintain the coolant temperature [24]. Ultimately this method is more suitable for an application such as the facility operated at INL where adequate funding and personnel is available.

3-D printing was explored by Scholz for PIV applications where Somos WaterClear® Ultra 10122 and RenShape® SL 7870 were used [25]. However, for those materials to become transparent a coating needed to be sprayed on the piece, as the part was opaque out of the printer. A low viscosity fluid was also difficult to find to match that index of the printed materials, where the closest would be either a 62.5% weight sodium iodide aqueous solution or a high zinc iodine concentration aqueous solution. The high zinc solution resulted in the solution being colored red and the sodium iodide solution suffered from yellow discoloration over time exposed to air, both discolorations impeding the clarity of the fluids.

The review by Hassan and Dominguez was consulted again and the materials examined were further examined resulting in PMMA being chosen as the solid. Choosing the optimal liquid between the 60% aqueous sodium iodide and the p-cymene was ultimately decided by a minimized level of discoloration. Goth examined the discoloration of sodium iodide when exposed to air in his thesis, and the choice to continue with p-cymene was explained there as well [26].

The choice of PMMA and p-cymene has been replicated in experiments by Nguyuen and has continued to be used for this project as it has continued. However, a new paring of materials have been explored by dos Santos where borosilicate glass, known as Pyrex commercially, was chosen and paired with D-limonene at a matching index of 1.47 at a much closer matching index at room temperature than PMMA and p-cymene where PMMA and p-cymene had a difference of index of 0.0004 the Pyrex and D-limonene matching difference is 0.0001 [27].

It was initially considered when this round of funding was obtained to possibly convert the facility over to a Pyrex and D-limonene pairing, when various glassblowing artists and professionals were contacted, many were not willing to attempt the complex wire-wrapped geometry and those that were willing to take on such a task were asking for amounts above $50,000. Due to the relatively rapid changing of the test section with various additions and high flow rates it was decided that replacing the PMMA rods and wires with Pyrex would not be cost effective and would ultimately overspend the budget on an option that may only marginally improve the facility while also increasing the fragility of the assembly as a whole.

Pressure and flow behavior measurements have been collected from this facility. Vaghetto discusses the pressure measurements obtained in the 61-pin wire-wrapped rod bundle, and those results were then compared and evaluated by Chen, eventually leading to the updating of Chen's CTD correlation [28] [29]. Two-dimensional two-component (2D2C) velocity measurements in axial planes, characterizing the flow in regions near the enclosure wall and interior subchannels were discussed by Nguyen and Goth [30]

[31]. Two-dimensional three-component (2D3C) stereoscopic PIV velocity measurements for the cross-flow area near the wall including some interior measurements were completed by Nguyen [32]. Goth also conducted a comparative study where Nek5000 numerical simulation results were compared to PIV experimental results, which found that maximum relative error between experiments and simulations were favorable at less than 10% [33].

3.3. Subchannel Blockage

Experimental and numerical studies by Chen, Merzari, Brockmeyer, Nguyen, and Goth show that the flow characteristics within the wire-wrapped fuel assembly are significantly complicated and strongly influence the flow mixing and heat transfer phenomena between the coolant fluid and fuel rods [34] [29] [35] [1] [30] [31] [26].

The hotspots, mentioned previously, when flow is impeded can lead to damage, component failure, and an overall reduced lifespan of the structural materials of the liquid metal flow loop. The materials that are damaged can erode away and collect inside of the fuel bundle creating these core blockages [36]. Some system codes were improved to acknowledge porous blockages in the 1990s such as the code by Oshima, ASFRE-III, but largely research on blockages has been almost wholly absent from wire-wrapped fuel assemblies. This could be in part from the generally complex flow of a wire-wrapped assembly, along with the previously incapable computational power that is now available to CFD users.

The local effects of these blockages are interesting to the research community as an anomaly from the traditionally considered unblocked assembly as the primary

operating condition of a reactor. However, that ideal condition in reality may be less of a reality and a case where various blockages do in fact exist in a reactor may be far more common. Due to the nature of a LMFBR having an opaque coolant and in a case in which it is virtually impossible to actually know what is exactly happening inside of the reactor it can be a very good approximation of reality when having some idea of the effects of the blockages on a reactors thermal-hydraulic behavior. Han comprehensively studied and postulated the effects of these blockages in his work at Oak Ridge National Lab in 1977 [36]. The lodging of debris and/or foreign material from broken wires or even failed pins are considered the most important causes of these blockages.

Pacio [37] has examined the effects of a solid blockage in an experimental setting at SCK CEN in Belgium using the MYRRHA facility in a 19-pin bundle and has found that temperatures did increase downstream from a blockage when compared to an unblocked subchannels of the same geometry. Outside of a wire-wrapped facility Piro has experimentally gathered three-dimensional, three component velocity fields in a CANDU reactor where the subchannels were blocked [38]. Piro did this utilizing magnetic resonance velocimetry (MRV), a relatively new and very different technique when compared to the PIV techniques commonly used. MRV does require the experimental facility to be composed of compatible materials similar to the necessity of MIR PIV, but does not require the use of tracer particles [38].

Unsteady RANS simulations by Di Piazza were used to examine blockage effects both locally and globally [39]. Jeong developed a model using a subchannel code to examine the effects of blockages in 2005 to examine the peak cladding temperature and

flow distributions in that scenario [40]. Chai [41] conducted CFD simulations exploring the effects of porous blockages that also supports the idea that a blockage would indeed increase the temperatures downstream from a blockage compared to an unblocked subchannel.

Overall there are limited experimental studies aside from Pacio and the studies completed recently that I did participate in by Nguyen that explore the effect of blockages on flow behavior in a wire-wrapped fuel assembly, and that lack of available data is what this work is focused on changing [42] [43].

4. FACILITY DESCRIPTION AND ALTERATIONS

The facility used here was originally designed and built by Nolan Goth and Phillip Jones during the first round of funding for research and development also funded by the DOE with teamwork with ANL, FRAMATOME, and TerraPower. The facility developed from this funding and effort is illustrated in Figure 1 (a) [26]. The facility is a MIR 61-pin wire-wrapped fuel assembly in a hexagonal test section all of which are made of poly (methyl methacrylate) (PMMA) utilizing p-cymene as a working fluid seen in Figure 1 (b). The index of refraction for PMMA and p-cymene is matching at about 1.49 for both at 20 degrees Celsius, with a difference of only 0.0004, an extremely small amount that is essentially negligible. An example of the matching index can be seen in Figure 1 (c). P-cymene has been a proven combination as a MIR fluid combination with PMMA and has been utilized in several other experimental facilities at Texas A&M University [7-15] [26] [30] [32] [22] [31] [33] [23] [44] [45] [42] [43].

4.1. Overview

The facility consists of three loops, a primary, secondary, and tertiary. The primary loop consists of a tank, pump, flow meter, PMMA central test section containing the PMMA 61-pin fuel bundle, upper and lower PMMA plena, and downcomer. The secondary loop also consists of a tank and pump along with a brazed plate heat exchanger that is the interface between the primary and tertiary loop. The tertiary loop consists of a pump and large cooling water tank that feeds into the cold side

of the heat exchanger. The primary and secondary loop pumps are controlled using a variable frequency drive (VFD) while the pump on the tertiary loop is operated at full frequency when in use.

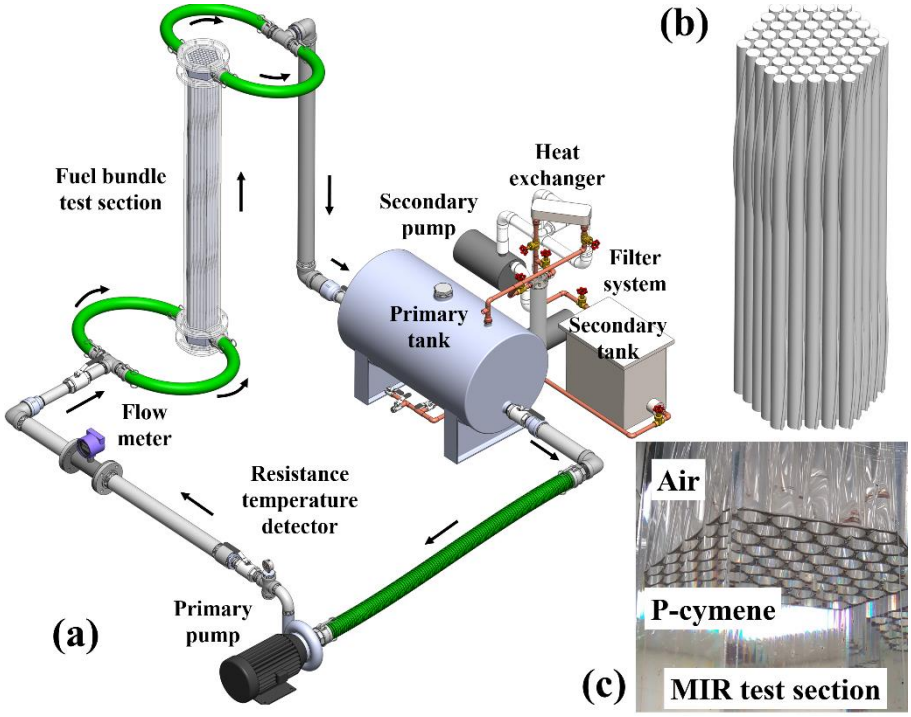

Figure 4.1 Overview of the test facility and example of MIR effect.

4.2. Materials

The majority of the experimental loop is constructed with stainless steel, whether that be the piping, fittings, or the tanks. There are three hoses that use cam-lock style connections and those hoses are flexible ultra-high-molecular-weight polyethylene (UHMWPE) which is known to be chemical resistant against organic solvents such as p-cymene. The test section is unlike the rest of the experimental facility as it is almost completely made of PMMA with the only pieces of a different material being the

stainless-steel nozzles for the cam-lock fittings. Surrounding the test section is an t-slot aluminum sub structure that the test section sits inside of allowing for quick modifications to be performed as needed. Outside of that aluminum substructure is a steel superstructure which provides a sturdy mounting point for the aluminum substructure to be anchored to as well as the upper plenum.

The test section contents of 61 wire-wrapped pins seen in Figure 4.1 (b) are fabricated in house using cast acrylic rods and extruded acrylic wires. The behavior of extruded and cast acrylic rods is discussed by Goth [26] and it was determined that cast acrylic was preferred due to the minimized impact of p-cymene on the structural integrity and characteristics of the acrylic. Extruded acrylic tends to absorb acrylic and deform over time. Due to the limitations associated with manufacturing these raw materials the best that can currently be done is purchasing the rods as cast acrylic and settling for extruded wires as they are too small to be cast.

4.2.1. Specification and Fabrication

The wire-wrapped assembly is scaled up by a factor of approximately 2.5. the P/D ratio was selected to be constant in the designation of the scaling of the assembly. The target P/D ratio was 1.189 previously determined by Goth. This P/D ratio lead to a full pitch of the wrapped rods being about 18.75 inches (476.3 mm) in length. The diameters of the rods and wires are 5/8-inch (15.875 mm) and 3 mm respectively. The wire-wrapped rods are fabricated individually by hand using cyanoacrylate based super glue as a bonding agent between the rods and wires.

The hexagonal enclosure has a wall width of 3.5 inches (88.8 mm), and with all 61 pins installed the hydraulic diameter, D_h, of the bundle is 7.7 mm. The axial length of the test section is equivalent to 3.5 wire pitches (1667 mm), ignoring inlet and outlet plena. The visualization region exists from 2.25 wire pitches to 3.25 wire pitches, allowing for approximately 139 D_h for flow to develop and 15.5 D_h for the outlet effects to be dissipated. An example of the visualization region used for the center blockage can be seen below in Figure 4.2.

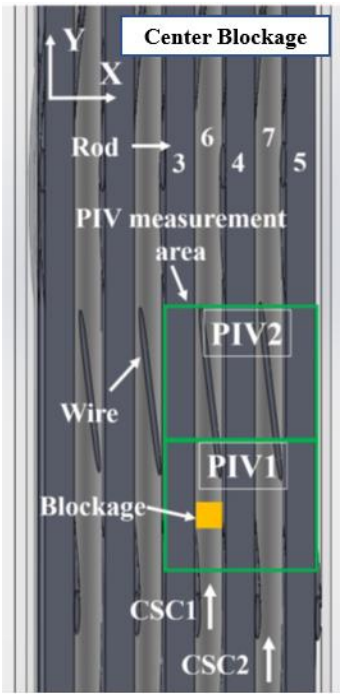

Figure 4.2 Visualization Region for Center Blockage

4.3. Blockage Fabrication

The blockages designed by Pacio and simulated by Chai were both porous blockages [37] [41]. Pacio's blockage was designed as a porous media surrounded by a

stainless-steel shell that would attach to the stainless-steel rods. Chai using a simulation decided to apply some porosity factor to the blockage geometries applied.

Fabrication of a porous blockage using PMMA would be a very difficult task as the porosity would need to be uniform and quantifiable. After much discussion it was decided that for optical transparency and experimental viability a solid PMMA blockage would be the best baseline experiment moving forwards for this experiment.

The blockages used in these experiments were taken from a decommissioned upper spacer plate that had been polished to be optically clear. The plate was cut using a Dremel tool and worked down to the dimensions to fit in an internal subchannel and another geometry for an exterior subchannel. An example of these blockages can be seen in Figure 4.3 below, along with the plate they were derived from.

Figure 4.3 Interior Blockage and spacer plate to offer a visual of how the blockage will interface with rods.

The locations of the blockages can be seen later in another figure where the laser planes are shown as well as the subchannels of interest, CSC1 and CSC2 for the center subchannels and ESC and for the exterior subchannels. The center blockage is located

1,184 mm above the entrance of the test section. The dimensions of the blockage are 12.7 mm in height, between 12.7 mm and 3.175 mm wide, and between 15.845 mm and 19.05 mm in length. The exterior blockage is located 1,241 mm above the test section entrance, with a height of also 12.7 mm, width of 12.7 mm, and length of 38.8 mm. an image of this exterior blockage can be seen below in Figure 4.4

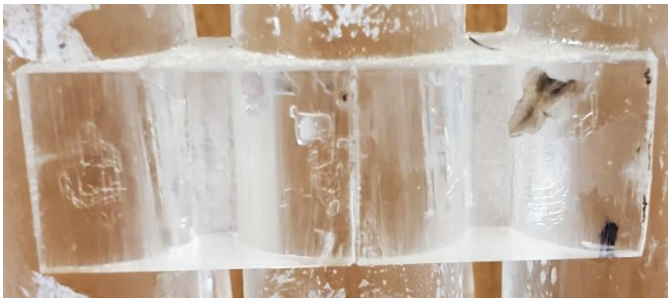

Figure 4.4 Exterior blockage attached to the three rods at Exterior 1

4.4. Alterations

Upgrades completed during the period encompassed in this thesis include several alterations that have streamlined operation of the experiment. First was the inclusion of a high accuracy pitot tube from OMEGA, model number FPT-6130, located past the test section on the downcomer, paired with two USB powered differential pressure transducers mounted in parallel, a ±10 inch of H_2O and ±2.5 PSI each with 0.5% accuracy of their respective range, to fully encapsulate the flow range of the facility.

Next was a replacement for the original it400 totalizer and turbine flow meter with an InnovaMass 240i vortex shedding flow meter from Sierra. That vortex shedding flow meter has an accuracy of 0.7% of the read value for flowrate and a 0.1 ℃ accuracy of the resistance temperature detector (RTD). Both the vortex shedding flow meter and pitot tube and transducers are capable of recording data for the flow rate of the facility. The flow meter wired directly to the DAQ used through a NI-9206 card using the 4-20 mA connections and the transducers into a computer through USB with their own software from OMEGA. The flow meter setup is more streamlined as the readings are available with the axial pressure readings while the transducers output pressure readings that are then converted to flow rate through the provided equation provided by OMEGA. However, the flow meter is able to report values for flows only above 25 gallons per minute (GPM), while the pitot tube is capable of recording much lower flow rates as well as the highest flowrate capable for the facility.

5. TR-PIV METHODOLOGY

PIV is a non-intrusive, laser based, optical measurement technique used to quantify velocity vector fields of a fluid of interest. The field is broken down into fluid elements where the displacement of a fluid element over a given time interval is the velocity of that fluid element. Capturing the displacement of these fluid elements is done by using highly reflective micro seeding particles that are neutrally buoyant with the fluid they are used in. The laser used reflects off of these particles and they stand out with high contrast with the rest of the fluid. This reflected light is captured by the CCD digital camera sensors to create an image. The cameras are capable of operating at various frequencies when capturing images, which allows the user to fine tune the displacement of the particles from image to image, with a desired displacement of no less than 5 pixels and no more than 15 pixels. Some assumptions necessary to be made for this measurement technique are that the seeding particles are homogeneously distributed throughout the fluid and that they match the behavior of the fluid perfectly on the scale of a fluid element.

5.1. Experimental Setup

The measurements acquired in this experiment are 2D2C measurements where the resulting data consists of flow fields in a two-dimensional plane. In previous experiments several planes were chosen to examine an unblocked 61-pin wire wrapped bundle, specifically what is referred to as Center 2 and Exterior 1. Center 2 bisects the center pin and two subchannels that are surrounded by four rods each and a total of 7 rods. In Figure 5.1 below rods labeled 1-7 are the surrounding rods for the center

subchannels CSC1 and CSC2, while rods 8-10 are the rods in contact with the exterior blockages in the wall subchannel ESC. These two different subchannel types are interior and edge subchannels, which provide very different flow behavior due to the inherent geometrical difference of the locations. In Figure 5.1 below it can be seen that the laser plane for the center 2 measurements for CSC1 and CSC2 have little space occupied by a wire, and are accurate of the location of the blockage, the exterior subchannel shoes wires occupying space. The edge subchannel actually measured actually does not have wires where the blockages are located, but do have wires at some point downstream from the blockages.

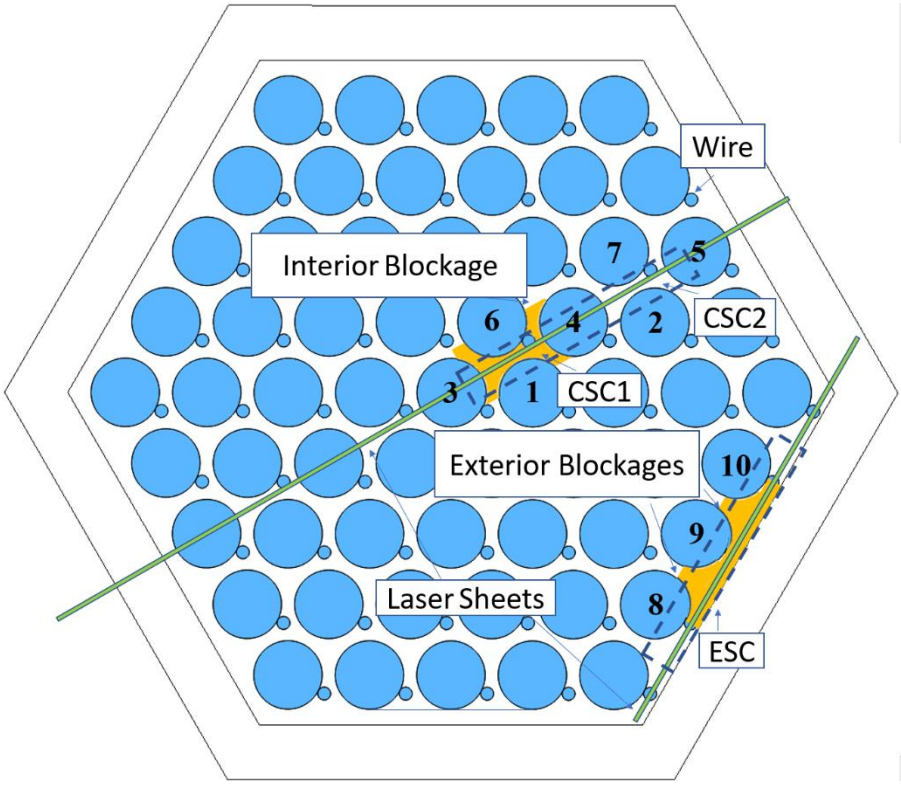

Figure 5.1 Center blockage and Exterior blockages and subchannels of interest with laser sheets for visualization.

The experiments conducted in the fulfillment of this thesis consist of measurements at three Re #, 4,000 and 17,000 for the exterior blockages and 4,000, 17,000 and 19,000 for the center blockage. The 17,000 and 19,000 Re #s represent fully developed turbulent flow, while the 4,000 Re # is closer to a turbulent flow that is still close to a transitionary region. After conducting measurements at the center with a single blockage it was determined that the necessity of reaching the higher Re # of 19,000 was not necessary to experience the effects of turbulence in the assembly. The decision to choose the target Re # stems from the convention used in the past experiments on this facility along with the flow regime in Figure 5.2 below from Cheng and Todreas [11]. Overlaid in this figure is the specific Reynolds numbers that are targeted for this experiment. It can be easily seen that both of the high Re #'s are close to one another, and they fall well within the turbulent region for this type of fuel bundle. The lower Re # is closer to the transition turbulent region, suggesting that the results from this Re # will be indicative of the behavior near that flow regime region.

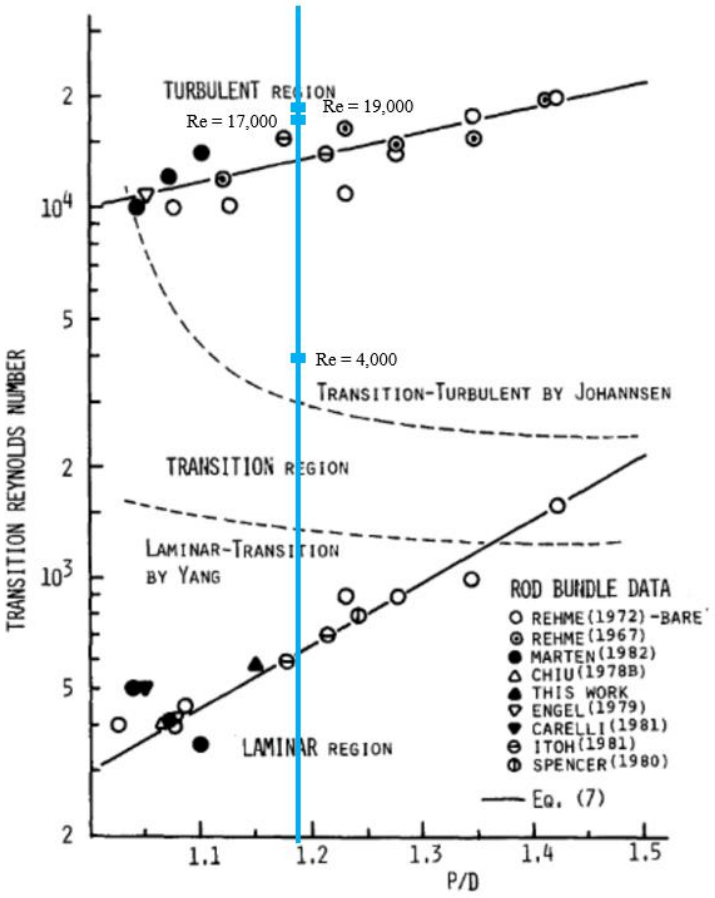

Figure 5.2 Flow regime chart for hexagonal fuel assemblies and Re #'s targeted in this experiment. Reprinted with permission from [11].

The center subchannels have a gap distance of 15.6 mm while the exterior blockages are located in the wall subchannels that effectively have no distinction between the subchannels. Therefore, a visual difference when observing the flow behavior in the wall subchannel will not be acknowledged.

The equipment used for this are two high-speed CMOS Phantom M310 cameras with Zeiss 105 mm camera lenses with f5.6 apertures. The Phantom M310 cameras are equipped with 1-megapixel sensors that output images with a resolution of 1280 x 800

pixels with a 12-bit image depth. Those cameras also contain 12 GB internal flash memory drives that save the images for short storage. Paired with these cameras is a 20 Watt continuous laser operating at a wavelength of 527 nm where the beam from the laser is passed through a collimator, 25mm, and 15mm optical plane lenses that narrow the beam down and then converts it to a plane of a thickness of 1.5 mm. Depending on the measurement either the camera side or laser side is passed through a correction prism that ensures that the laser plane and cameras are perpendicular to one another. An example of this can be seen below in Figure 5.3 for the center blockage. An overview of the

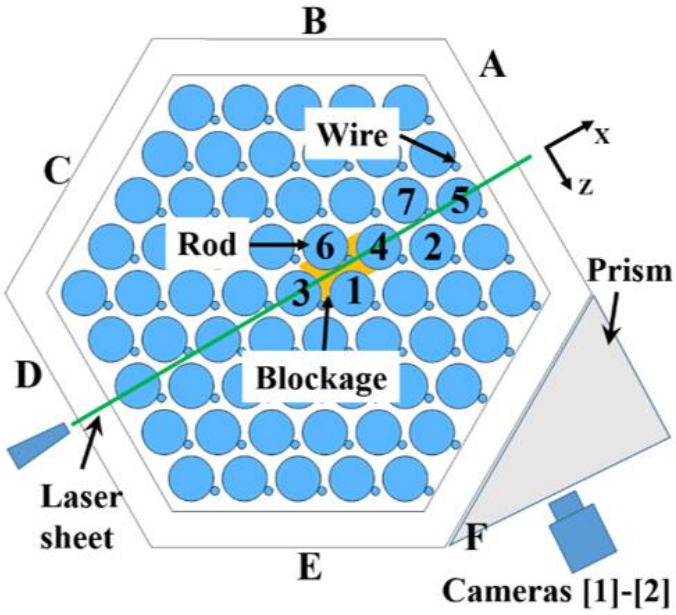

Figure 5.3 Center blockage, laser, and camera geometry

The laser and cameras are both mounted on traversing systems that allow precise movements of both the laser and cameras. The laser was mounted on a two-axis vertical and horizontal traverse system while the cameras were mounted on a three-axis travers

allowing for vertical, horizontal, and depth control rather than utilizing the camera focus. The reason for this three-axis system was to limit the change of field of view for the cameras as they change focal length inside of the fuel assembly. The orientation of the cameras is important as they need to have some overlap for the image captured by each camera. This is checked before data is acquired to ensure the run is of substance. An example of this setup can be seen in Figure 5.4, where a correction prism can also be pictured.

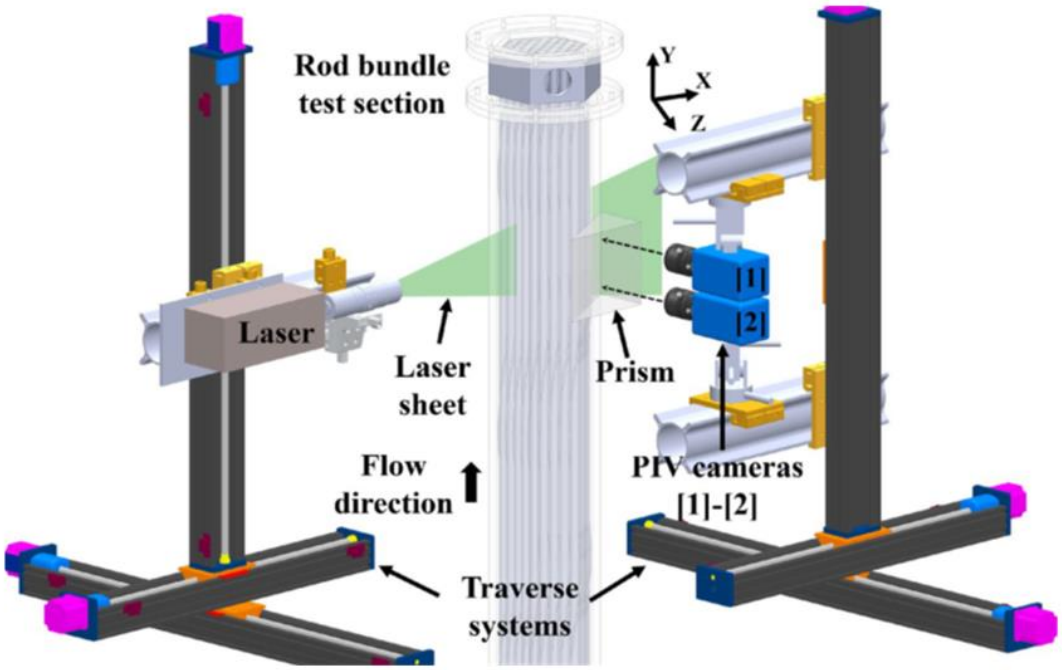

Figure 5.4 Experimental traverse, laser, and camera setup

The seeding particles used for the PIV measurements are silver-coated hollow glass spheres that are pre-mixed in the primary tank and then circulated throughout the flow loop. This ensures that the seeding particles are entirely mixed and present in the

test section during experimentation. The particles are left in the flow loop for the majority of the time, including downtime and maintenance, but on occasion will be filtered out when the silver begins to tarnish and the fresh particles will be injected through a syringe port just past the pump.

5.2. Data Acquisition

The target Re #s do have corresponding primary pump frequencies that do recreate the same flow behavior so long as the facility is kept relatively similar. The pump frequencies used were 11.47 Hz, 51.5 Hz, and 58 Hz for the Re #s of 4,000, 17,000, and 19,000 respectfully. The pump is brought up to this speed and the facility is allowed to run for approximately 10 seconds to ensure a steady state operation for the test.

The phantom cameras use a proprietary software to control the recording of the cameras, and they are also triggered with a simple pulse generator. The pulse generator ensures that the measurements begin at the same time for both cameras. Simultaneously when the cameras are recording the flowrate, temperature, and pressure measurements are recorded using a data acquisition unit as mentioned before.

The Re #s were calculated by taking the reading of the flowmeter and converting to a bulk mean velocity, U_m. Knowing the density of the p-cymene to have a nominal density, ρ_{pcy}, of 855 kg m^{-3} at 20°C that can be adjusted by the recorded temperature, and the dynamic viscosity, μ_{pcy}, of 8.1 x 10^{-4} Pa s, which was also adjusted for temperature, the Re # could be calculated with the below equation.

$$\boldsymbol{Re} = \frac{(\boldsymbol{U_{mean}} * \boldsymbol{D_h}) * \boldsymbol{\rho_{pcy}}}{\boldsymbol{\mu_{pcy}}} \quad (5.1)$$

The camera frame rate frequencies, f, used are different depending on the target Re #. The frequencies used were $f = $ 800 Hz for the 4,000 Re # tests, and $f = $ 2,800 Hz for the 17,000 and 19,000 Re # tests. Fine tuning adjustments are made for each test, including exposure and gain of the cameras to ensure the best possible images. That frame rate is then used to calculate the interframe time delay by simply taking the inverse of the framerate as can be seen below.

$$\delta t = 1/f \tag{5.2}$$

This resulted in time delays of approximately 12.5 x 10^{-4} s and 3.6 x 10^{-4} s for the respective frame rates. This time delay allows for the seeding particles to displace themselves at a maximum of less than 15 pixels per image.

During each measurement three videos were captured, where each video consists of 8309 frames. When a Re # was complete the files were offloaded from the flash storage on the cameras onto either an external HDD or onto a computer's local storage, whether that be a HDD or SSD. The cameras operate on a network, so speed for transfer can reach the theoretical limit of 1 Gb/s, however, the read and write speeds of the drives they are saving to are the limiting factors. For this experiment an external HDD with a 4 GB capacity was used to safely store the video files. After the files are transferred the camera flash storage can be cleared and more videos can be recorded.

After image capture for the particular day a calibration image is needed, usually a short .cine file rather than a full-size measurement. A calibration image requires the use of a piece of equipment known as a calibration plate. The plate used here is from the

company LA Vision and has very tight tolerances for both the dot spacing and overall construction. The thickness of the plate is within ±0.02 mm, dot spacing within ±0.02 mm, and level of separation between ±0.01 mm [46]. These high tolerances allow for the images taken for that particular experimental setup to have a known reference to compare the pixel sizes with known measurements. This is done by placing this calibration plate at the same distance of the laser plane from the cameras. Along with having the plate at the same distance away from the camera, it is essential to ensure that the same thickness of material between the cameras and calibration plate is achieved. I.E. if there is 5 inches of material between the camera and laser plane at an index of refraction of 1.49, such as PMMA and p-cymene, there needs to be 5 inches of material at an index of refraction of 1.49 between the camera and calibration plate. This should be the last thing done for a particular measurement set, however, this should be done after every measurement set if possible, as many factors can alter the exact setup of cameras and laser plane such as an accidental push or nudge when someone is walking past the experiment, or even movement when turning on and off the laser and cameras.

5.3. TR-PIV Pre-Processing

The cameras record a series of images as a .cine file for each run and that .cine file is extracted as a set of .tif files at a 12-bit depth for each image. Other image bit depths are options, but the coding software used, MATLAB, is capable of working with 12-bit images, so the native depth of the cameras is preferred. An example of a raw image can be seen below in Figure 5.5.

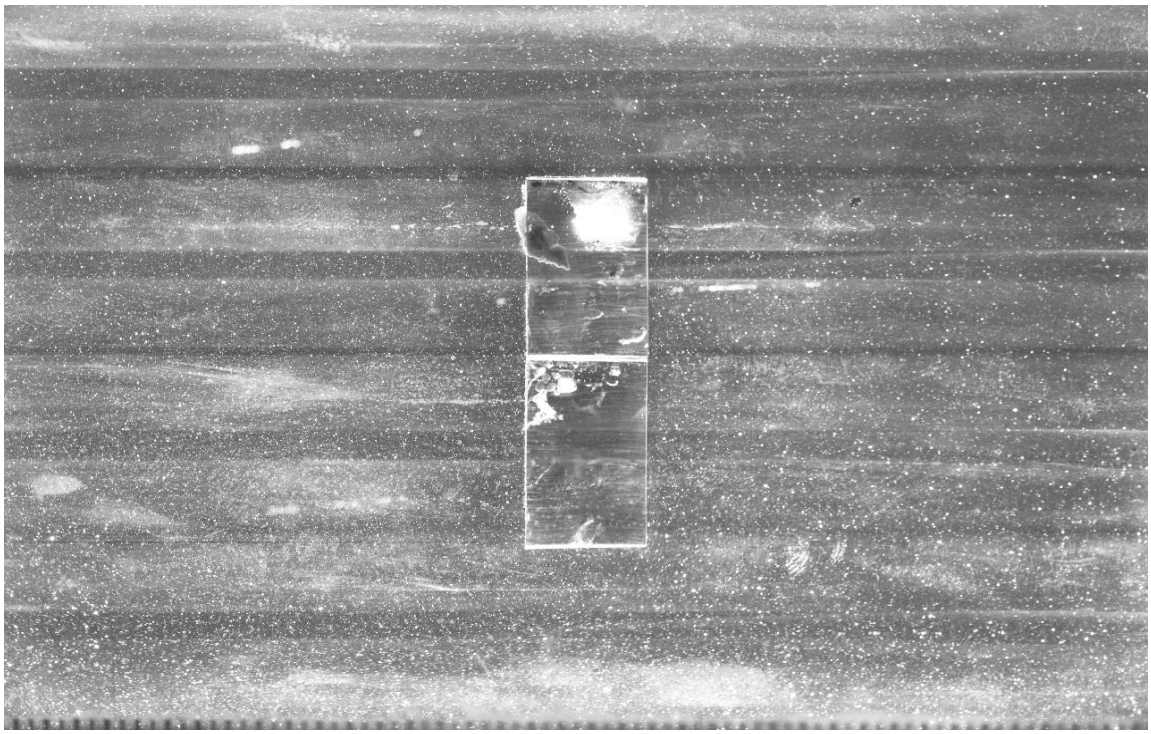

Figure 5.5 Raw PIV image at a Re # = 4,000

Once those images are extracted from the .cine files into .tif files, the next step is to perform a background mean. Each .cine file is treated as a separate directory and MATLAB is used to load in each image as a matrix. Each sequential image is added into that original matrix and once every file in that directory is loaded in and added, a mean is performed by dividing those images by the total number of images in that directory. That resulting matrix is then saved as another 12-bit .tif image file. A sample background mean is seen below in Figure 5.6.

Figure 5.6 Background mean image for the same camera and same Re # as the previous image (contrast and brightness altered for thesis).

Those background mean images together with raw images are then used to create a static mask. Those masks are created using a software called Image-J. The usual process of this is drawing the shape of known objects in the view of the image and deleting them out of the image. Afterwards using a threshold adjustment tool in Image-J, erroneous parts of the image can more finely be eradicated and a static mask can then be formed as a binary image of values 0 or 255, masked or conserved respectfully. A static mask is seen below in Figure 5.7.

Figure 5.7 Static mask image generated using Image-J and the background mean image

Those background mean images and static masks are then used to edit the raw .tif files for each directory. Each file is loaded in, the background image is subtracted out from the raw image and then the mask is multiplied out where the zero values override any values that may have been left over after background subtraction. Images at this point may be oversaturated, which can be corrected by dividing the image by a factor of 2, as the photos operate on a binary scale. The resulting image can be seen below in Figure 5.8.

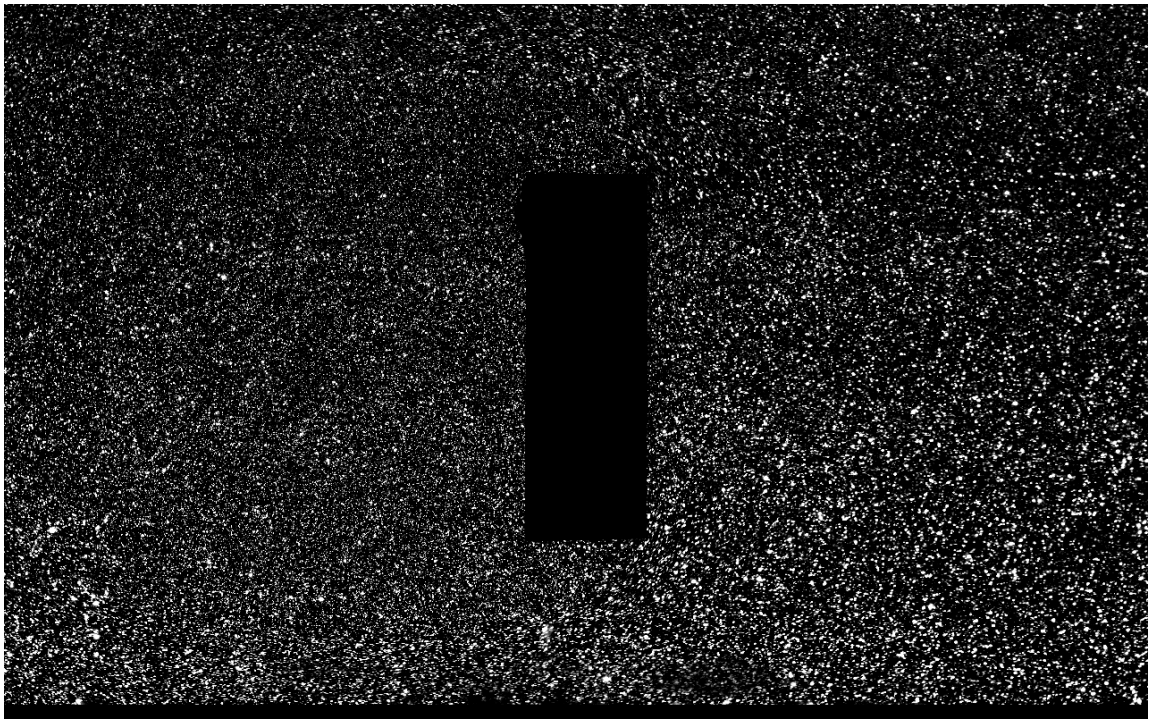

Figure 5.8 Background subtracted and masked image ready for PRANA processing

After these steps the images are ready for processing using an in-house PIV code developed by Eckstein and Vlachos [47]. This code has been applied in several recent studies by Nguyen, Goth, and dos Santos [23,26,27,30,31,32,33,42,43,44,45].

5.4. PRANA

PRANA is an in-house PIV code that is an advanced multi-pass, multi-grid PIV code. Cross correlation between each frame is performed by using a robust phase correlations (RPC) algorithm. This algorithm substantially reduces bias errors and peak locking effects when high shear and rotational motion is present, when compared to the standard cross correlation algorithms.

The statistical cross-correlation between images is used to estimate particle-image displacement. The reason for using this cross correlation is that attempting to track every particle instead would be computationally expensive, or even impossible. A method that does attempt to track every particle is particle tracking velocimetry (PTV), which is much more involved and was not used in this particular experiment. However, PTV has been used in the past by Goth and Nguyen in order to analyze the flow behavior in subchannels that were much smaller than the regions of interest in this experiment, where using a PIV approach would not be an appropriate method.

Consecutive images in this method are treated as pairs, where the first image is discretized into several windows determined in the graphic user interface (GUI) of PRANA. These windows begin at relatively large pixel grids with the expectation that a particle would have a maximum displacement of 25% of this window. The search window in the second image in the pair is a larger size than the interrogation window of the first image. These sizes are determined by the gridding done in the beginning of the processing. In the first image there are unique particle-images that are captured and then searched for in the second image. The displacement of these particle-images is determined and used to create a vector. The number of vectors in the results is dependent on the grid chosen, where a finer grid will produce more vectors, however, the resolution of the grid is better small only when the particles have realizable movement between the pair of images. PRANA is able to locate these structures by taking the image pairs and converting them over to a spectral domain using fast Fourier transform (FFT). The

average intensity of an interrogation window can be calculated in the equation below. The figure of merit for the cross-correlation is found in the equation following.

$$\bar{I}_a = \frac{1}{B_x B_y} \sum_{k=1}^{B_x} \sum_{l=1}^{B_y} I_a(k,l) \tag{5.3}$$

$$R(i,j) = \frac{\sum_{k=1}^{B_x} \sum_{l=1}^{B_y} (I_a(k,l) - \bar{I}_a)(I_b(k+i,l+j) - \bar{I}_b)}{\left[\sum_{k=1}^{B_x} \sum_{l=1}^{B_y} (I_a(k,l) - \bar{I}_a)^2 \sum_{k=1}^{B_x} \sum_{l=1}^{B_y} (I_b(k+i,l+j) - \bar{I}_b)^2\right]} \tag{5.4}$$

There is an assumption that shear between adjacent fluid elements is ignored, and this is accomplished by ensuring the interrogation window is small. This is essential because the displacement resulting from the cross-correlation is actually an average of the group of particle-images within the interrogation window.

The interrogation windows of this experimental data set were started at 64 x 64 pixels and end at 32 x 32 pixels. Three passes were iterated, and the initial and final iterations possessed 50% and 75% of window overlap respectively. Velocity vectors were calculated from the correlation maps, and subpixel displacements were obtained using a Gaussian peak fit [48] [49] [50]. Vector validation was completed using a universal outlier detection approach proposed by Westerweel was used to identify and replace erroneous vectors between PIV iterations [51]. By using velocity bicubic interpolation, those erroneous vectors were then replaced. The space for the final adjacent vectors was found to be 0.68 mm.

The static mask discussed before is used to also define a region of interest (ROI) in which the locations that are masked do not undergo a computational effort, therefore saving time and resources, and ultimately speeding the process up for both PRANA processing and post-processing of results.

Post-processing in PRANA involves three passes of decreasing the grid size using a Multigrid-Discrete Window Offset (DWO) and robust phase correlation (RPC) algorithm. The choice of three passes here align with the three passes for data disseminated from this project by Nguyen and Goth [42] [43] [32] [31]. A DWO increases the cross-correlation accuracy by offsetting the interrogating window between passes by an equal amount of integer-pixel-displacement [52]. Increasing the accuracy allows for the initial pass to be coarse compared to the final pass, reducing the total computational cost, thus speeding up the process. This coarse first pass is operated on by a velocity interpolation function, bi-cubic interpolation, which develops the initial guess required for the next pass. This bi-cubic interpolation function uses a uniform grid and three points per polynomial, and then produces the smoothest result. That smoothed result is the superior result when compared to other built-in velocity interpolation functions. This smooth interpolation is essential for establishing the Multigrid-DWO method.

A more detailed discussion of how the RPC algorithm works is necessary for understanding the principals behind the PRANA code being used in this research. RPC works by spatially discretizing each image into multiple interrogation windows and applying an FFT to each window to transform that window to the spectral domain. Each image pair are cross-correlated and a phase transform filter is applied to increase the amplitude of the correlation peak, while the product of that transform filter is multiplied by a weighted signal-to-noise ratio (SNR) in order to reduce the amplitude of the noise. This essentially defines the peaks more than would normally be noticed by simply an

FFT, or even an FFT and phase transform filter, and is similar to a background subtraction of raw images in lay-terms. After these things are applied an inverse FFT is applied to each interrogation window and the correlation peak is operated on by a three-point Gaussian estimator to increase the probability of peak identification [52]. After the correlation peak is identified the displacement is only known as an integer pixel value, while the subpixel displacement is estimated by a three-point gaussian estimator, the most commonly used method. A correlation peak maximum is determined by using a Gaussian curve and passing the peak through three points in both the X and Y directions.

A validation check is performed after each pass to eliminate vectors that don't necessarily agree with the average behavior of the other vectors calculated. These odd vectors can be caused by in and out of plane loss of particle-image pairs, or even by steep velocity gradients. This validation check is the universal outlier detection, which operates by comparing the magnitude of a grid of vectors neighboring a selected vector, and examining the median value of those neighboring vectors. If the selected vector is outside of that median value, it is replaced. This process is done for every vector in the neighboring grid.

5.5. TR-PIV Post-Processing

The output files from PRANA are .mat files containing several variables. The variables of interest for this thesis were the X and Y values of the location and the U and V components of the velocity vectors. The output file from PRANA has only pixel values for the location values for variables X and Y, and the U and V components are reported as vectors in pixels as well. Converting these variables to usable information

requires a conversion from pixels to some unit of distance relevant to the experiment, in this case pixels to mm. This was done by taking an image where a known distance was available to observe in the image. The blockage in these images were of a known thickness of 0.5 inches or 12.7mm, and the length of the blockage was measured with Image-J and was found to be 151 pixels in height. A simple conversion of pixels to mm was done by dividing the width, 12.7 mm, by the number of pixels, 151, and multiplying both the location matrices, X and Y by that factor. Alternatively, and more universally excepted, a calibration plate such as the LaVision calibration plate mentioned before can be used, where the tolerances of the plate size and dot location is very tight and reliable. The velocity matrices, U and V, have to be multiplied by another factor that also includes the frequency of the camera, as U and V from the raw results only are the length of the vectors in pixels. This factor is the width, 12.7 mm, divided by the height, 151 pixels, then multiplied by the camera frequency, either 800 or 2,800 Hz, depending on the target Re # of the particular experimental run.

The utilization of two cameras stacked on top of one another allows for the total window to be increased. However, there is some additional processing necessary to make this choice useful. A calibration plate was mentioned before, and is very useful in this situation where mapping can be done between the two camera's PRANA results and they can easily be remapped over each other. However, this was not the case for this experiment, and the remapping was done in another method. When looking at raw images from the two cameras at the same frame, a unique identifier in both images was chosen and the location was marked. The X and Y components for this unique identifier

are then adjusted so that in each image that identifier would share the same coordinates. This augmentation of the X and Y variables in the .mat PRANA output allows for the results from both cameras to be combined.

Once the results are combined from the top and bottom cameras the next step is linearizing the data and creating a master matrix. This is done by taking each U and V matrix and linearizing it. This is done for all PRANA results in a directory, creating a large matrix, in this case a size of around 24,927 X 28,908 for both U and V each. This large matrix .mat file is around 10 GB in size, but is much more convenient to work with than having to access an entire directory of files. From this large matrix several statistical results can be calculated. These include ensemble-averaged vertical and horizontal velocity components, U_m and V_m, the RMS vertical and horizontal components, ${u'}_{rms}$ and ${v'}_{rms}$, and the Reynolds shear stress, $\overline{u'v'}$.

5.5.1. Ensemble Averaged U and V Components

An ensemble averaged value is different than a time-averaged value. A time-averaged component would be more impacted by the random nature of that specific measurement cycle. In this experiment three separate experimental runs were obtained for every Re #, and those three different runs are all averaged together, thus creating a sample size that is less dependent on time than a time-averaged sample group. The governing equation for this can be found below.

$$\mu_{X(t)} = \int_{-\infty}^{\infty} x * p_{X(t)}\ (x)dx \tag{5.5}$$

Where μ is the mean of some component X, here either U or V, that changes with time, and $p_{X(t)}$ is a probability density function. This can be accomplished by also using the equation for a simple average below, due to the inherent nature of the data used.

$$\mu = \frac{1}{N}\sum_{i=1}^{N} A_i \tag{5.6}$$

Where A_i is either the U or V component from the PRANA results. When a component has gone through this process of averaging, a representative value of the waveform is seen for the ensemble averaged matrix.

5.5.2. Root-Mean-Squared fluctuating U and V Components

RMS is also known as the arithmetic mean of the squares of a set of numbers, or a quadradic mean. The Root-Mean-Squared fluctuating U and V components are similar to that of a standard deviation, even sharing in the same governing function overall for this data set as is seen below.

$$U'RMS = \sqrt{\frac{1}{N-1}\sum_{i=1}^{N}|U_i - \mu_U|^2} \tag{5.7}$$

$$V'RMS = \sqrt{\frac{1}{N-1}\sum_{i=1}^{N}|V_i - \mu_V|^2} \tag{5.8}$$

The reason that this value is not referred to as a standard deviation is because it is used as a comparison to the baseline mean values found in the ensemble average, rather than some value independent of the actual mean. This value provides the insight needed to understand where in the flow behavior the average values are changing most often. This indicates the regions in which there may be more turbulence, and in further analysis possibly higher order flow structures.

5.5.3. Reynolds Shear Stress

The Reynolds shear stress is calculated by taking the U and V components and subtracting from each value the mean component U_m or V_m and then multiplying each of those instantaneous values together. A mean is then completed on those multiplied values to result in our average Reynolds shear stress. The equation that governs this can be seen below.

$$\overline{U'V'} = \frac{1}{N}\sum_{i=1}^{N}(U'_i * V'_i) \tag{5.9}$$

Where

$$U' = U - U_m \tag{5.10}$$

And

$$V' = V - V_m \tag{5.11}$$

A Reynolds shear stress has the units of velocity squared rather than the units of stress in this case. The shear stress can help identify the regions in which there is large momentum transfer, suggesting a region that is undergoing a significant amount of turbulence. The contour plots of this are often well correlated with the regions of U'RMS and V'RMS components, dominated by whichever is having a larger effect. It should be noted for the flows seen in these experiments where flow has a dominant vertical direction, the shear stress is often the largest where the horizontal component, U'RMS, is the highest.

6. PIV RESULTS AND DISCUSSION

The experimental runs completed for this thesis consist of two planes, the center 2 plane and exterior 1 plane as seen in Figure 5.1. The general convention for these images is that the flow is positive in the y-direction and x-direction from bottom to top and left to right respectively. This follows a general quadrant 1 scheme on a 2-D plane. Three Re #s were targeted for the center plane, 4,000, 17,000, and 19,000, while two Re #s, 4,000 and 17,000, were targeted for the exterior 1 plane. The choice of these Re #s was discussed previously, but in short, the lower Re # represents a Transition-Turbulent flow behavior, while the 17,000 and 19,000 both represent fully turbulent flow behaviors. The data associated with these Re #s have been fully pre-processed, PRANA processed, and post processed. These results will be discussed in this chapter, beginning each section with the center 2 plane and ending with the exterior 1 plane for each component. First and second order statistics will be examined as the mean velocity vector fields and magnitude contours of the mean vertical and horizontal velocity, RMS fluctuating vertical and horizontal velocities, and Reynolds stress.

6.1. Ensemble-Averaged Vertical Velocity Components

Ensemble-averaged vertical velocity components are reported as velocities in m/s, representing the mean flow structures for a particular data set. In this case the vertical components are the primary flow direction, therefore the values here will be higher than the horizontal components discussed later. These mean contours provide a visualization of the major flow behavior in the primary flow direction, specifically the impact of the blockages on the bulk velocity in these subchannels.

6.1.1. Center 2

The vertical component of the ensemble averaged velocity at the center 2 plane at various Re #s can be seen below in Figure 6.1. In this figure it can be seen that the maximum velocity vector values increase as Re # increases from 4,000 to 19,000. It is present in this figure that the flow patterns in CSC1 are altered when compared to CSC2 by the blockage present in CSC1. The color contour shows that for all Re #s the flow is significantly lower in the axial direction in CSC1 than in CSC2. In CSC1 there is a stagnation region where the axial flow impinges upon the leading edge of the blockage, and a recirculation region downstream of that blockage. The effect of the blockage is effectively the same between the Re #s 17,000 and 19,000 with the largest difference being the overall magnitude of the velocity, where the flow structure is very similar. The lower Re # does show some difference in flow structure, but there is still that stagnation region and recirculation. This reduction of the axial velocity demonstrates that the blockage does have a significant impact on the flow behavior in an interior subchannel. The reduction in velocity would indicate a lowered heat transfer rate at this location, coinciding increasing the temperature near the blockage. This behavior supports the findings of both Pacio and Chai [37] [41].

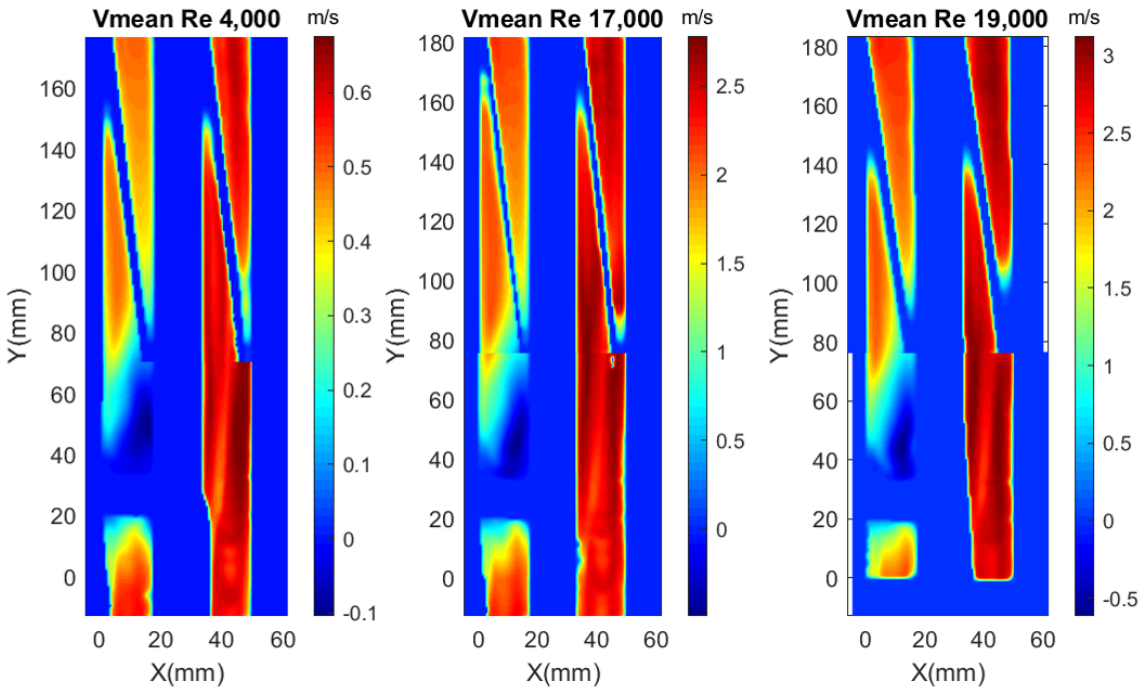

Figure 6.1 Ensemble-averaged vertical velocity components for Center 2 plane, CSC 1 (left) CSC2 (right)

6.1.2. Exterior 1

The ensembled-average vertical velocity contours for the exterior 1 flow plane can be seen in Figure 6.2 below. The flow structures between the two Re #s, 4,000 and 17,000 are very similar in overall shape. The main difference between the two is the significant magnitude increase form a maximum vertical velocity of just above 0.6 m/s and near 2.5 m/s in the positive y-direction for Re = 4,000 and 17,000 respectively. There are apparent stagnation regions on the sides of the blockage and right on the leading edge of the blockage. After the blockage and on the sides, there are recirculation regions that are significant in size.

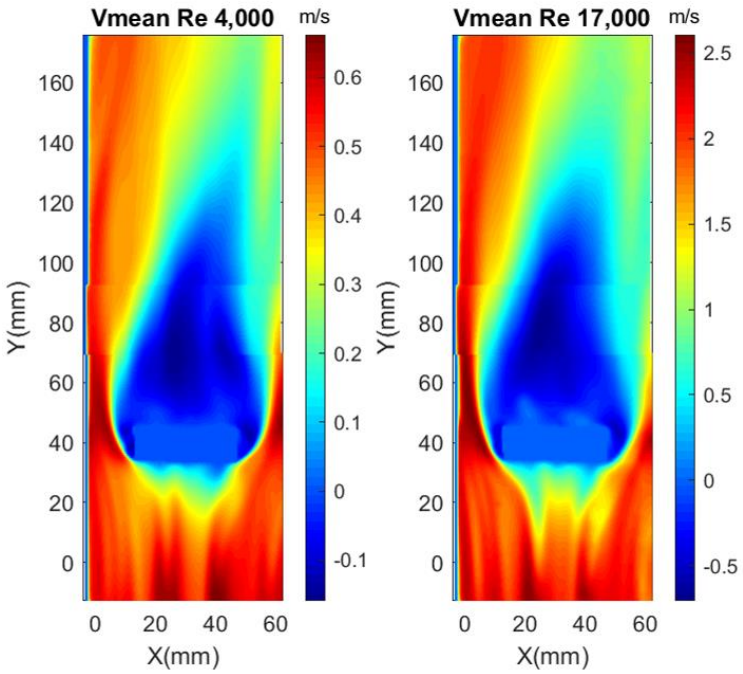

Figure 6.2 Ensemble-averaged vertical velocity components for exterior 1

With maximum recirculation of 0.1 m/s and 0.5 m/s in the negative y-direction for Re = 4,000 and 17,000 respectively. This recirculation and overall reduction in velocity suggests that the heat transfer capability at this blockage would indeed reduce the heat transfer capability in this region resulting in a local hotspot.

6.2. RMS Vertical Velocity Component

The RMS vertical fluctuating velocity is the variation, in m/s, that each vector deviates from the mean velocity value in that direction, in this case the axial direction. This statistical value can help the observer understand how certain elements in the flow effect the behavior and impact the stability of the flow.

6.2.1. Center 2

It can be seen in Figure 6.3 that as the Re # increases up to 19,000, the RMS fluctuating velocity becomes larger over all, with specific impact near the blockage.

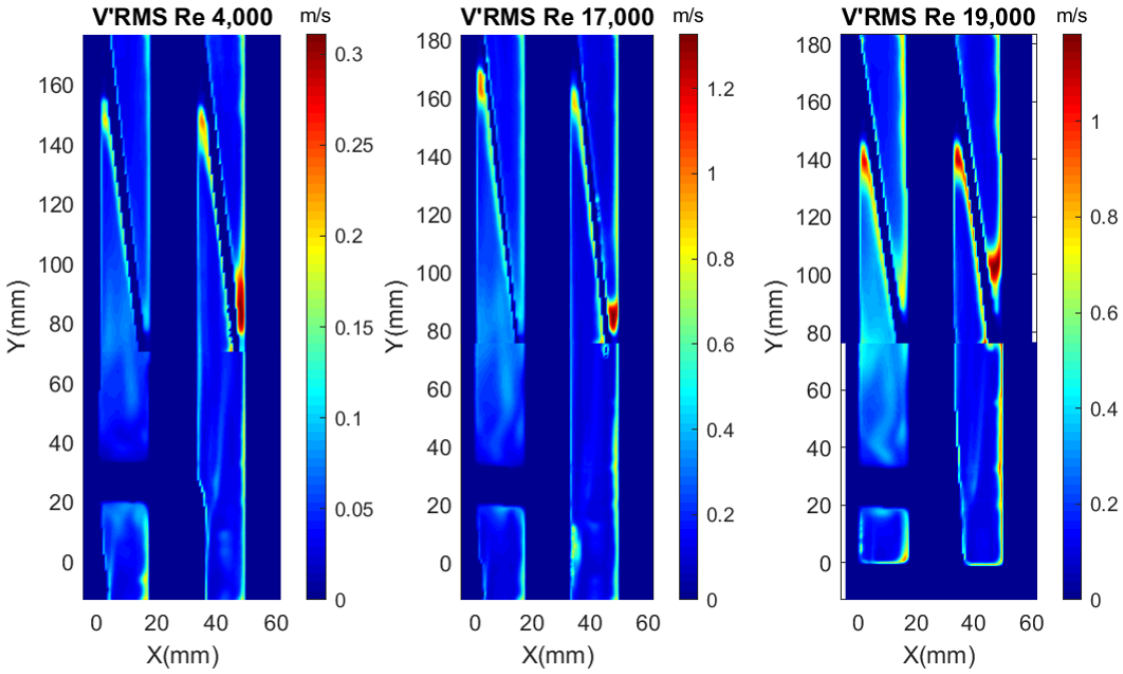

Figure 6.3 RMS vertical fluctuating velocity component for Center 2 plane, CSC1 (left) CSC2 (right)

Before the blockage, for Re = 4,000, the RMS value is larger than the other regions surrounding the blockage. The RMS also increases significantly after the blockage when Re = 19,000. RMS values are highest near the wire locations, most likely due to changes in direction near those locations, or possibly effects from interaction with the rods and wires behind the plane.

6.2.2. Exterior 1

The RMS vertical fluctuating velocity contours, seen in Figure 6.4, for the exterior 1 plane is more interesting than the center 2 plane, specifically for the higher Re # of 17,000.

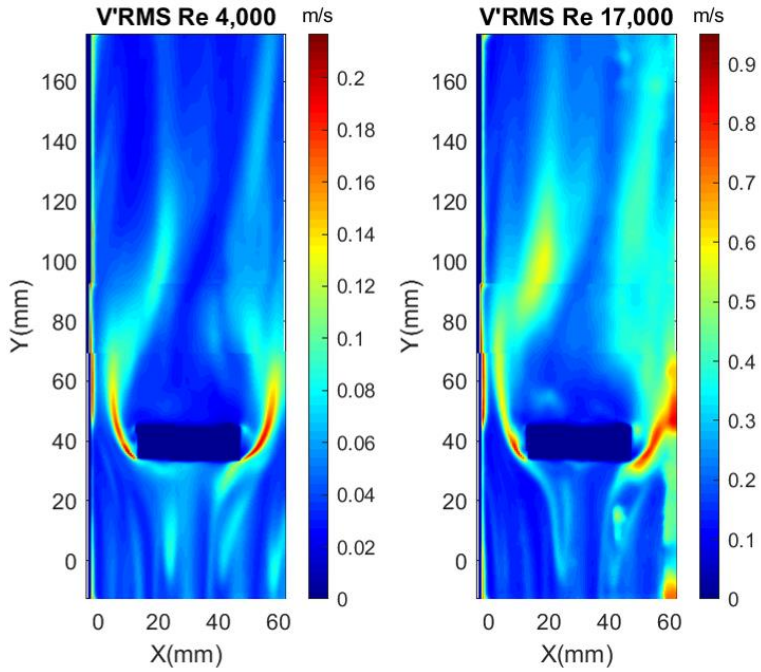

Figure 6.4 RMS vertical fluctuating velocity component for Exterior 1 plane

It is important to note that there are high fluctuations near the sides of the blockage and downstream as the flow would begin to return to normal. These large values suggest that there is a high level of impact from the blockage on flow structures near and downstream from the blockage, leading to very unpredictable and turbulent flow in those regions.

6.3. Ensemble-Averaged Horizontal Velocity Components

The ensemble-averaged horizontal velocity components are similar to the vertical components, although are focused in the experiment as the less dominant flow direction. It will be seen that there is more of a variation with positive and negative values as the flow does go in both left and right directions and those directions don't necessarily indicate a deviation from the main flow behavior in the vertical direction, but will exist on more of a dichotomy than the previously examined vertical flow path. Values of zero in these contours suggest that the flow is primarily in the vertical direction. Reynold's stress will be discussed later and will pair the observations for the vertical and horizontal mean velocities together to have a greater understanding of the flow behavior.

6.3.1. Center 2

Throughout the majority of the contour areas seen in Figure 6.5 there is some horizonal component to the mean flow, however the maximum value in those contours has an absolute value of 0.5 m/s, significantly lower than the vertical flow component maximum of 3 m/s in the interior subchannel CSC 2 seen in Figure 6.1 for Re = 17,000. The bulk of the fluid can be seen in the contours to follow the direction of the wires. However, near the blockage there are structures in all Re #s that suggest some time of rotation that is occurring both before and after the blockage. This is not seen in CSC2, while in CSC1 it is very prevalent. The degree of this motion is very different between the high and low Re #s, as would be expected with significantly different flow rates, the more turbulent flows having higher values at a more concentrated area, while the lower Re # seems to have a larger region of less intense horizontal flow.

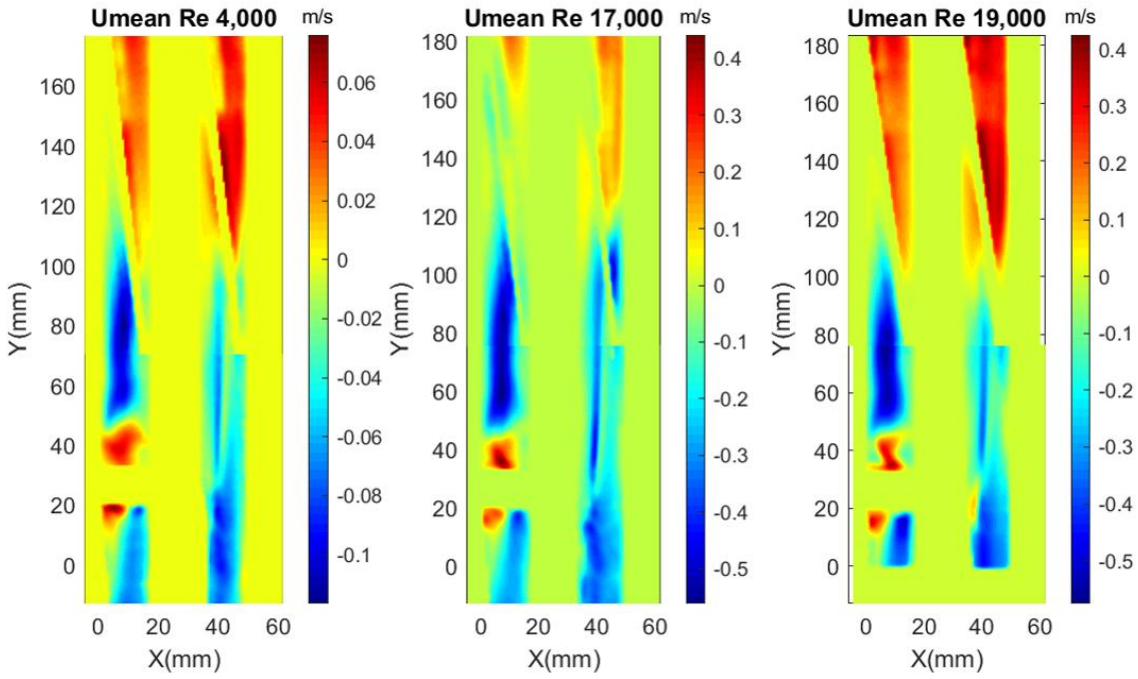

Figure 6.5 Ensemble-averaged horizontal velocity components for Center 2 plane, CSC 1 (left) CSC2 (right)

6.3.2. Exterior 1

The contours in Figure 6.6 demonstrate very predictable flow behavior where flow passing by the blockage would favor the paths of least resistance, negative in the x-direction for the left side of the blockage and positive in the x-direction for the right side of the blockage. Aside from the immediate effects of the blockage there is a noticeable trend of the flow following the shape of the bundle, after flow has stabilized downstream from the blockage, where the flow begins to favor what would be a counter clockwise flow, following the clocking angle of the pins. This behavior is expected near edge and wall subchannels as there is less mixing and more of a bulk flow behavior.

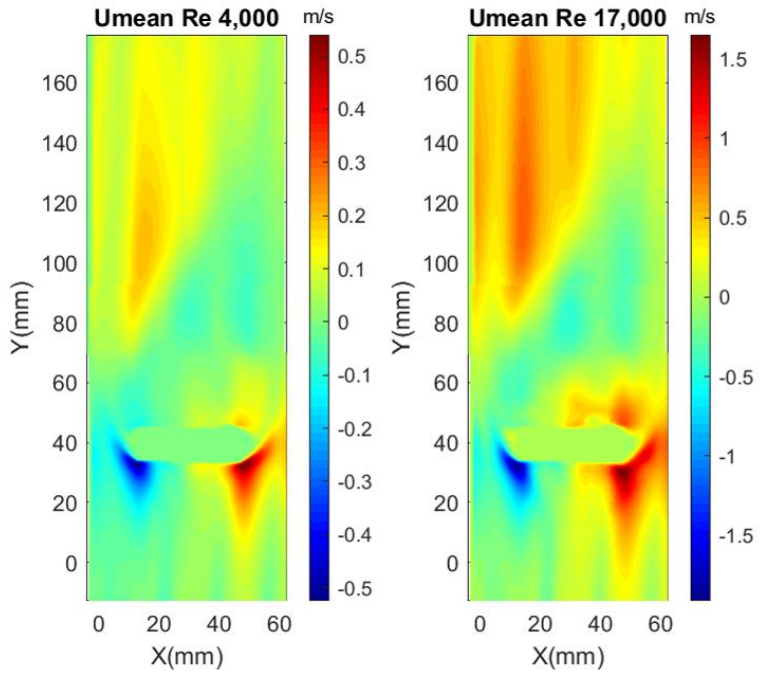

Figure 6.6 Ensemble-averaged horizontal velocity components for Exterior 1 plane

6.4. RMS Horizontal Velocity Component

The RMS horizonal velocity contours are representative of the variability seen in the flow over time. A high value here would indicate that flow in this region is not predominantly favoring either the positive or negative x-direction, suggesting a large variability in the flow behavior. With lower Re #s these values are smaller as the flow behavior is more predictable, and with higher Re #s these values can increase substantially.

6.4.1. Center 2

There is a structure that is interesting in the contours seen in Figure 6.7 beginning after the blockage in CSC1 and following down the subchannel to the interaction of the wire. There seems to be a noticeably raised level of fluctuation near the wire for all Re

#s, but significantly more, by a factor of 5, for the higher Re #s than the lower Re #. It would be expected that as the flow becomes more developed the RMS values would reduce, and that is seen in CSC2 where the overall values are lower in that subchannel comparing the higher Re #s to the lower Re #. However, the introduction of the blockage introduces significantly more variability in the flow behavior relatively. This would imply that cooling in this region would not be consistent and could result in a hotspot downstream from the blockage, after the recirculation region. The recirculation region seems to be causing this based on the distance between the blockage and this region being past that region, and the recirculation region having a significantly lower RMS value.

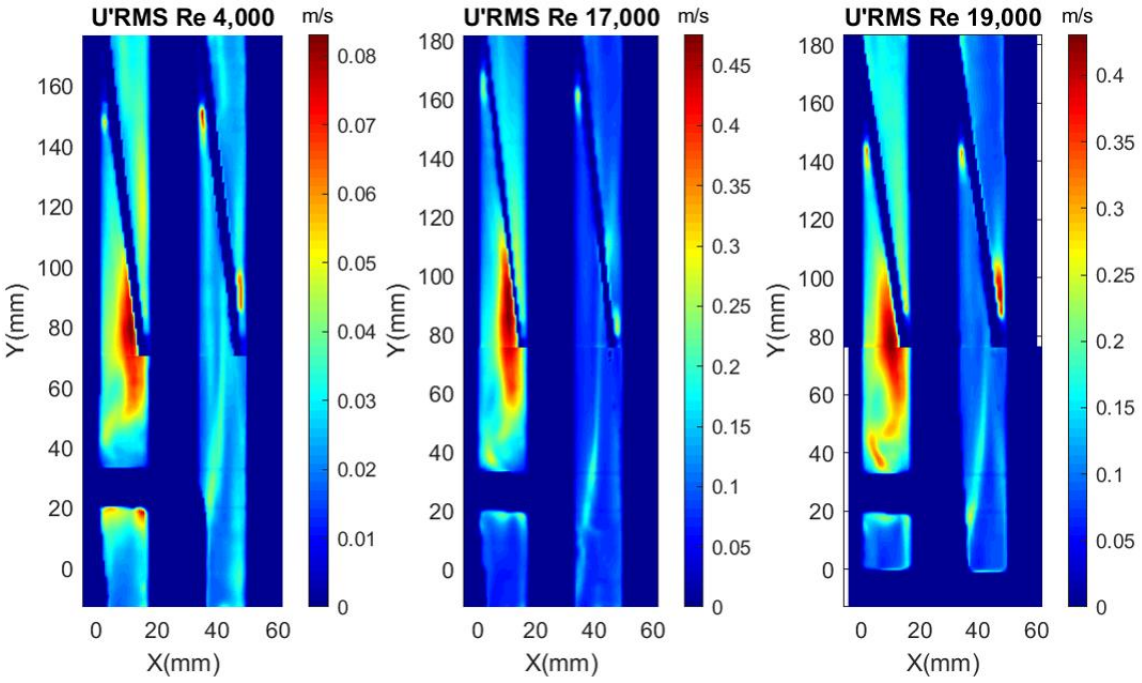

Figure 6.7 RMS horizontal fluctuating velocity component for Center 2 plane, CSC1 (left) CSC2 (right)

6.4.2. Exterior 1

The exterior 1 U' RMS values here in Figure 6.8 are on a similar scale to the center 2 values, however, they seem to be increased by about a factor of 2. The larger blockage size could account for this, however the majority of the area in these contours are of a lower magnitude, with the highest values existing on the lower corners of the blockage. At the lower Re # the behavior is similar between the left and right sides with a slightly higher variance on the right lower corner. The behavior at the higher Re # is significantly different where down steam of the blockage is highly variable, and the variance overall favors the right side near the blockage and downstream the left side is favored with higher RMS values.

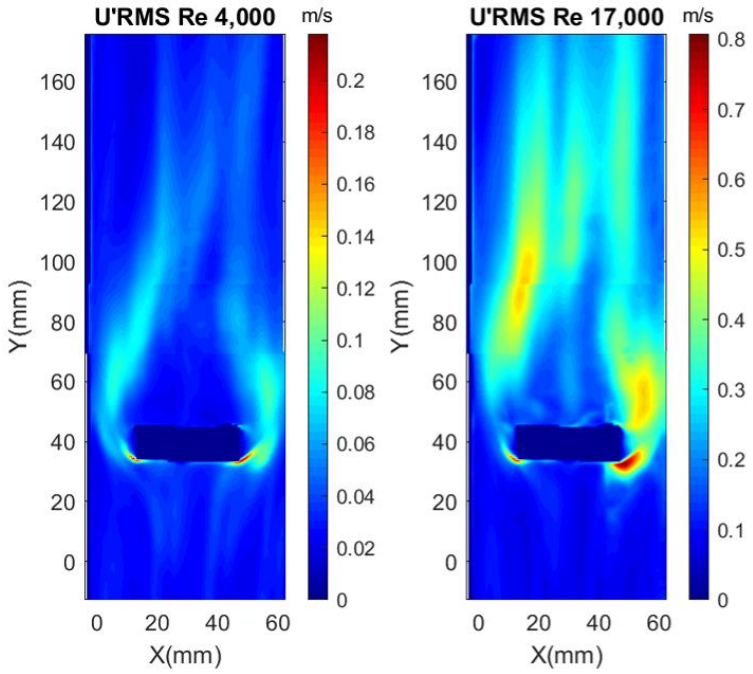

Figure 6.8 RMS horizontal fluctuating velocity component for Exterior 1 plane

While these values are high, they are somewhat expected after examining the behavior in center 2 at CSC1. The impact of the blockage seems to extend beyond the immediate recirculation region into the reconstruction of the flow into a fully developed flow. This would suggest that a blockage of this larger size at the exterior would have a significant effect on cooling, leading hotspots downstream from the blockage extending past a recirculation region, similar to the behavior seen in CSC1 in center 2.

6.5. Reynold's Shear Stress

These Reynold's Shear stress contours visualize the momentum transfer in the flow structures. Lower values are associated with less turbulent regions, and higher with more turbulent regions. It should be noted that the only truly zero regions in these contours are where no flow is occurring, I.E. the blockage or rods between subchannels. Other near zero regions simply have less turbulent behavior, there for less shear stress.

6.5.1. Center 2

The contours of Reynold's shear stress for center 2, seen in Figure 6.9, the stress for the lowest Re # is over an order of magnitude lower than either of the high Re #s. This is relative to the overall turbulence in the flow, where the lower Re # falls closer to a transition turbulent region compared with the fully turbulent other Re #s. This pattern indicates the recirculation region downstream from the blockage, and the structures seen in these contours fall well in line with the same structures seen in the RMS contours of Figure 6.3 and Figure 6.7. The primary direction of this flow is in both the positive y and x directions, with only a small amount favoring the negative x direction and positive y direction.

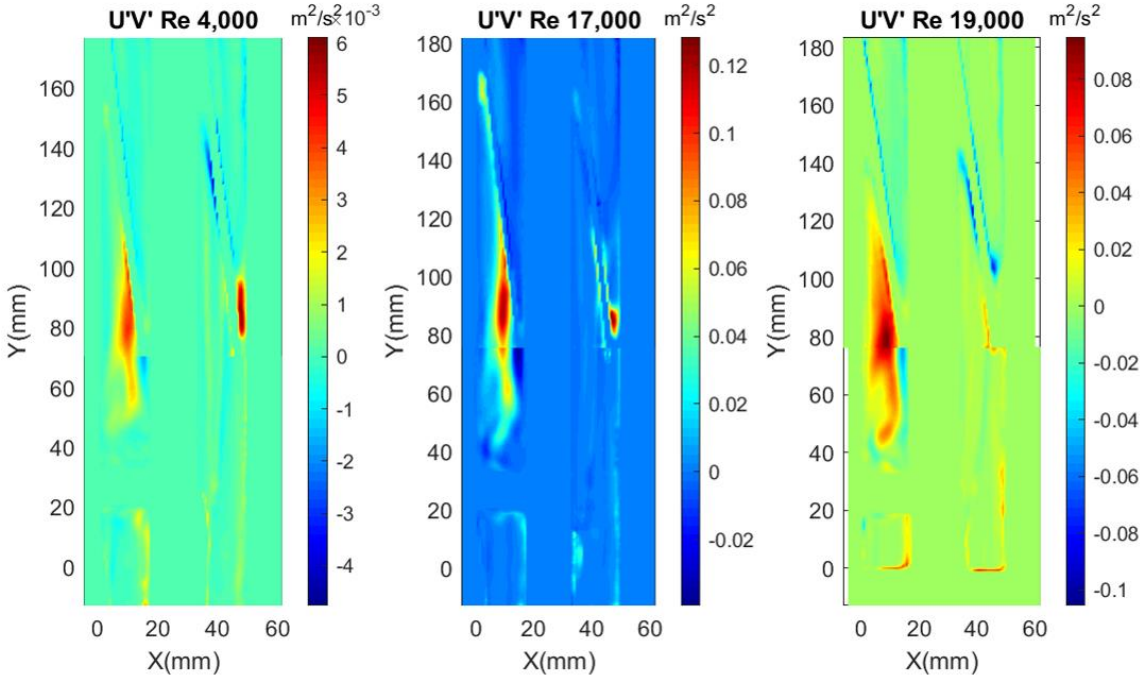

Figure 6.9 Reynolds stress component for Center 2 plane, CSC1 (left) CSC2 (right)

6.5.2. Exterior 1

Reynold's stress contours in the Exterior 1 edge subchannel can be seen in Figure 6.10. These contours exhibit behavior similar to the RMS contours in Figure 6.4 and Figure 6.8 where the majority of the stress is located downstream from the blockages, and just before the blockages near the corners. The lower Re # has significantly less shear stress present, at around an order of magnitude gap between the high and low Re #. The high and low Re #'s shear stress contour peaks both at the lower corners of the blockage, and again downstream of the blockage, around the recirculation region. The recirculation region is similar to the single blockage in the CSC1 for the center plane, but is much larger. The shear stress contours also trend in the direction of the flow in the positive x and y directions.

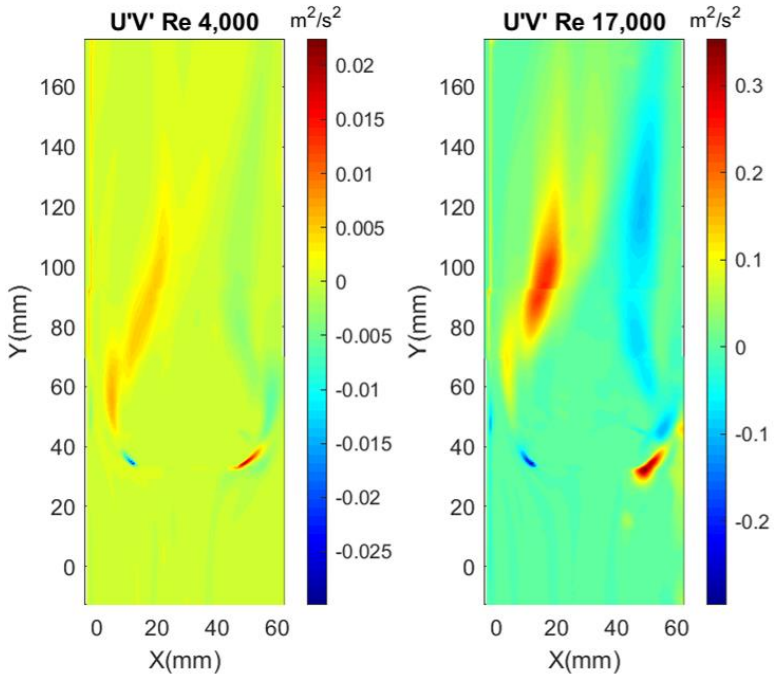

Figure 6.10 Reynolds stress component for Exterior 1 plane

6.6. Uncertainty

The uncertainty and convergence studies were not completed by myself, however the data collected in this thesis was also analyzed by Nguyen and some of those findings will be mentioned and briefly discussed [42] [43]. It was found that for PIV processing of experimental runs, the percentage of vectors that would be considered bad, defined by the total number of vectors that failed validation in the final pass averaged over the total number of PIV velocity fields was between 3% to 4%. The lead to an uncertainty of the velocity measurements of about 0.1 pixel. PIV uncertainty propagation was carried out by using Sciacchitano and Wieneke's method of uncertainty propagation to estimate uncertainties of computed PIV statistical results [53]. Those statistical results including mean velocity, room-mean-square (RMS) fluctuating velocity, and Reynolds stress. The

uncertainties shown here in Table 6-1 were calculated by Nguyen in a work encompassing the same data presented in this thesis for subchannels CSC1 and CSC2, however, for the exterior edge subchannel, ESC, uncertainty was not quantified [42] [43].

Table 6-1 Estimated uncertainties e_{Re1} and e_{Re2}, for statistical results of CSC1 and CSC2

	U/U_m (%)	V/U_m (%)	u'_{rms}/U_m (%)	v'_{rms}/U_m (%)	$u'v'/U_m^2$ (%)
CSC1					
e_{Re_1}	0.16	0.43	0.11	0.30	0.03
e_{Re_2}	0.28	0.58	0.20	0.41	0.04
CSC2					
e_{Re_1}	0.09	0.45	0.06	0.32	0.03
e_{Re_2}	0.14	0.58	0.10	0.41	0.03

The values in Table 6-1 are maximal and are normalized by the mean velocity U_m. Error is difficult to quantify in these measurements as experimental parameters such as processing algorithms, calibration, laser pulse delay, particle seeding density, out-of-plane particle displacement, interrogation window, and cross-correlations algorithms are all subject to interrogation. Studies by Sciacchitano and Neal discuss this in length [54].

7. CONCLUSIONS

An experiment exploring the impact of blockages on flow behavior within a 61-pin wire-wrapped fuel bundle in a hexagonal duct, the prototypical geometry of an LMFBR nuclear reactor, was discussed in this thesis. The facility used in this experiment was the product of the first round of research for a MIR 61-pin wire-wrapped fuel bundle in a hexagonal duct, funded by the DOE and partnered with several nuclear industry leaders. That facility uses p-cymene as a working fluid paired with PMMA to reach a matched index operation. Some improvements were made on the facility in preparation for this experimentation with the intention of smoothing out the operation of the facility during experiments.

The consensus of the effect of a blockage in an LMFBR prior to this work was that it will cause hotspots on the fuel pins downstream from those blockages. Experiments and CFD simulations were conducted by other authors in order to gain some knowledge for the impact of a blockage, however, a visualization-based experiment has not been attempted prior to the experiment that this thesis is composed around. Pacio found through experimentation with the MYRRAH facility at SCK-CEN in Belgium that there will indeed be hotspots downstream from the blockage [37]. Chai found similar results with their CFD simulations exploring the effect of various blockage geometries that were porous [41]. A decision was made to create blockages out of non-porous PMMA, the same MIR material as the rest of the facility, to conduct baseline experiments and characterize the flow behavior with simple geometries for subchannel

blockage. Both blockages were manufactured by hand from an existing decommissioned upper plenum spacer plate.

Two vertical planes were chosen from the existing data collected for an unblocked wire-wrapped fuel bundle, Center 2, a plane passing through the center pin of the bundle, and Exterior 1, the plane passing through an edge subchannel near the wall. The Center 2 plane consisted of two subchannels, CSC1 and CSC2, while the Exterior 1 subchannel is a large edge subchannel. The blocked subchannel in Center 2 was CSC1 and CSC2 was left unblocked. Exterior 1 doesn't necessarily exist as separate subchannels, so the blockage exists as two separate pieces that fit together to create the blockage used for this experiment.

The Center 2 blockage case was completed first and videos were captured for three Re #s. After examination it was decided that only two Re #s were necessary so for Exterior 1, only two Re #s were captured. Those Re #s were 4,000 and 17,000 for Exterior 1 and 4,000, 17,000, and 19,000 for Center 2. Two Phantom M310 high-speed CCD cameras paired with a 30-Watt continuous laser were used to capture the PIV images in this experiment. Images at a 12-bit depth were extracted from the resulting videos. Those images were pre-processed with MATLAB and were analyzed using PRANA, an in-house software based in MATLAB yielding results that were ultimately plotted using MATLAB. First and second order statistics were resolved from these results including ensemble averaged velocities for the U and V components, RMS velocity components for U and V, and the Reynold's shear stress.

The results from these measurements suggest that the effect of a blockage does align with the findings of Pacio and Chai, where a blockage does impede flow, resulting in what would be recirculation regions, allowing that fluid in that location to heat up more, creating a localized hotspot [37] [41]. The lower Re # for both the Center 2 and Exterior 1 experiments produced significantly smaller recirculation regions, and the flow seemed to be somewhat less impacted by the inclusion of a blockage. Although, for the higher Re #s, the blockage created significant recirculation regions and rotational motion downstream from the blockages, including significant shear stress at the edge of those recirculation regions. The Center 2 blockage had sizably smaller recirculation regions than the Exterior 1 blockage due to the significantly different size of the blockage. The exterior blockage also was less impacted by surrounding physical structures like rods and wires since it was along the wall.

This experiments that this work was derived from has come to result in two publications where this author is listed as a second author, and future work is planned to continue with the application of blockages of various geometries and the effect they have on pressure drop. Accompanying those experiments will be PIV measurements for new geometries. A porous blockage may be explored at some point in the future as 3-D printing advanced.

This work is expected to increase the data available as reference for RANS and LES CFD researchers to validate for flow behavior. As the database of experimental data grows this work will be added, with the ultimate goal of understanding the flow behavior

of LMFBR reactors to increase the life and safety levels required to advance energy into the next age of nuclear energy production.

REFERENCES

[1] L. Brockmeyer, L. B. Carasik, E. Merazi and Y. A. Hassan, "Numerical simulations for determination of minimum representative bundle size in wire wrapped tube bundles," *Nuclear Engineering and Design,* vol. 322, no. 1, pp. 577-590, 2017.

[2] M. Mathiew, K. Duggan and T. Galioto, "Heated bundle test in areva nps fuel cooling test facility," in *ANS Winter 2016 Conference*, 2016.

[3] B. Mays, "Experimental data sets for cfd calculations of flow and heat transfer in deformed assemblies," in *ANS Winter 2016 Conference*, 2016.

[4] P. Fischer, J. Lottes, Siegel A and G. Palmiotti, "Large eddy simulation of wire-wrapped fuel pins I: hydrodynamics of a single pin.," in *Proceedings of M and C+ SNA*, 2007.

[5] A. Saxena, U. Bieder, T. Cadiou and S. Viazzo, "Large eddy simulation of turbulent flow in a wire wrapped fuel pin bundles cooled by sodium," in *Advancements in Nuclear Instrumentation Measurement Methods and Their Applications,* 2013.

[6] W. D. Pointer, P. Fischer, A. Siegel and J. Smith, "RANS-based CFD simulations of wire-wrapped fast reactor fuel assemblies," in *International Congress on Advances in Nuclear Power Plants*, 2008.

[7] R. Collingham, W. Thorne and J. McCormack, "Coolant mixing in a fuel pin assembly utilizing helical wire wrap spacers," *Nuclear Engineering and Design*, vol. 24, no. 3, pp. 393-409, 1973.

[8] J. Lorenz and T. Ginberg, "Coolant mixing and subchannel velocities in an LMFBR fuel assembly," *Nuclear Engineering and Design,* vol. 40, no. 2, pp. 315-326, 1977.

[9] E. H. Novendstern, "Turbulent flow pressure drop model for fuel rod assemblies utilizing a helical wire-wrap spacer system," *Nuclear Engineering and Design,* vol. 22, no. 1, pp. 28-42, 1972.

[10] K. Rehme, "Pressure drop correlations for fuel element spacers," *Nuclear Technology*, vol. 17, no. 1, pp. 15-23, 1973.

[11] S. K. Cheng and N. E. Todreas, "Hydrodynamic models and correlations for bare and wire-wrapped hexagonal rod bundles — Bundle friction factors, subchannel friction factors and mixing parameters," *Nuclear Engineering and Design,* vol. 92, no. 2, pp. 227-251, 1986.

[12] I. Ahmad and K. Y. Kim, "Flow and convective heat transfer analysis using RANS for a wire-wrapped fuel assembly," *Journal of,* vol. 20, no. 9, pp. 1514-1524, 2006.

[13] S. Rolfo, C. Peniguel, M. Guillaud and D. Laurence, "Thermal-hydraulic study of a wire spacer fuel assembly," *Nuclear Engineering and Design*, vol. 1, no. 243, pp. 251-262, 2012.

[14] R. Gajapathy, Velusamy K, P. Selvaraj and P. Chellapandi, "CFD investigation of effect of helical wire-wrap parameters on the thermal hydraulic performance of 217 fuel pin bundle," *Annals of Nuclear Energy,* vol. 77, no. 1, pp. 498-513, 2015.

[15] E. Mezari, P. Fischer, H. Yuan, K. Van Tichelen, S. Keijers, J. De Ridder, J. Degroote, J. Vierendeels, H. Doolaard and V. Gopala, "Benchmark exercise for fluid flow simulations in a liquid metal fast reactor fuel assembly," *Nuclear Engineering and Design,* vol. 298, no. 1, pp. 218-228, 2016.

[16] N. G. Rasu, K. Velusamy, T. Sundararajan and P. Chellapandi, "Simultaneous development of flow and temperature fields in wire-wrapped fuel pin bundles of sodium cooled fast reactors," *Nuclear Engineering and Design,* vol. 1, no. 267, pp. 44-60, 2014.

[17] J. H. Jeong, J. Yoo, K. L. Lee and K. S. Ha, "Three-Dimensional flow phenomena in a wire-wrapped 37-pin fuel bundle for sodium fast reactors," *Nuclear Engineering and Technology,* vol. 5, no. 47, pp. 523-533, 2015.

[18] G. E. McCreery, H. M. McIlroy, K. D. Hamman and H. Zhang, "Design of wire-wrapped rod bundle matcehd indes-of-refraction experiments," in *16th International Conference on Nuclear Engieering*, 2008.

[19] M. Nishimura, H. Sato, H. Kamide, H. Oshima, K. Nagasawa and Y. Imai, "Investigation on velocity distribution around the wrapping wire in an inner subchannel of fuel pin bundle," in *20th International Conference on Nuclear Engineering and the ASME 2012 Power Conference*, 2012.

[20] H. Sato, J. Kobayashi, H. Miyakoshi and H. Kamide, "Study on velocity field in a deformed fuel pin bundle: Influence of pin deformation and wrapping wire on velocitry distribution," in *16th International Conference on Nuclear Engineering*, 2008.

[21] E. E. Dominguez-Ontiveros and Y. A. Hassan, "Non-intrusive experimental investiagation of flow behavior inside a 5 x 5 rod bundle with spacer grids using PIV and MIR.," *Nuclear Engineering and Design,* vol. 239, no. 5, pp. 888-898, 2009.

[22] Y. A. Hassan and E. Dominguez-Ontiveros, "Flow visualization in a pebble bed reactor experiment using PIV," *Nuclear Engineering and Design,* vol. 238, no. 11, pp. 3080-3085, 2008.

[23] D. T. Nguyen, E. Kappes, S. King, Y. A. Hassan and V. Ugaz, "Time-resolved piv measurements in a low-aspect ratio facility of randomly packed spheres and flow analysis using modal decomposition," *Experiments in Fluids,* vol. 59, no. 8, p. 127, 2018.

[24] C. Penreco, "White mineral oil product specifications," Calumet Specialty Products Partners L.P., 2016.

[25] P. Scholz, I. Reuter and D. Heitmann, "PIV measurements of the flow through an intake port using refractive index matching," in *16th International Symposium on Applications of Laser Techyniques to Fluid Mechanics.* , 2012.

[26] N. E. Goth, DESIGN AND PIV MEASUREMENTS ON A WIRE-WRAPPED 61-ROD HEXAGONAL FUEL ASSEMBLY EXPERIMENTAL FACILITY, College Station: Texas A&M University, 2017.

[27] A. A. C. dos Santos, M. Childs, T. D. Nguyen and Y. Hassan, "Convergence study and uncertainty quanitification of average and statistical PIV measurements in a matcehd refractive index 5 x 5 rod bundle with mixing vane spacer grid," *Experiemntal Thermal and Fluid Science,* vol. 102, no. 1, pp. 215-231, 2019.

[28] R. Vaghetto, P. Jones, M. Childs, S. Lee, D. T. Nguyen and Y. A. Hassan, "Pressure measurements in a wire-wrapped 61-pin hexagonal fuel bundle," *Journal of Fluids Engineering,* vol. 140, no. 3, p. 031104, 2018.

[29] S. Chen, Y. Chen and N. Todreas, "The upgraded cheng and todreas correlation for pressure drop in hexagonal wire-wrapped rod bundles," *Nuclear Engineering and Design,* vol. 335, no. 1, pp. 356-373, 2018.

[30] D. T. Nguyen and Y. A. Hassan, "Steroscopic particle image velocimetry measurements of flow in a rod bundle with a spacer grid and mixing vanes at a low reynolds number," *International Journal of Heat and Fluid Flow,* vol. 67, no. 1, pp. 202-219, 2017.

[31] N. E. Goth, P. Jones, D. T. Nguyen, R. Vaghetto, Y. A. Hassan, N. Salpeter and E. Merzari, "PTV/PIV measurements of turublent flows in interior subchannels of a 61-pin wire-wrapped hexagonal fuel bundle," *International Journal of Heat and Fluid Flow,* vol. 71, no. 1, pp. 295-304, 2018.

[32] D. T. Nguyen, N. E. Goth, P. Jones, L. Saya, V. Rodolfo and Y. A. Hassan, "Stereoscopic piv measurements of near-wall flow in a tightly packed rod bundle with wire spacers," *Experimental Thermal and Fluid Science,* vol. 92, no. 1, pp. 420-435, 2018.

[33] N. E. Goth, D. T. Nguyen, V. Rodolfo, Y. A. Hassan, A. Obabko, E. Merzari and P. Fischer, "Comparison of experimental and simulation results on interior subchannels of a 61-pin wire-wrapped hexagonal fuel bundle.," *Nuclear Engineering and Design,* vol. 338, no. 1, pp. 295-304, 2018.

[34] S. Chen, N. Toreas and N. Nguyen, "Evaluation of existing correlations for the prediction of pressure drop in wire-wrapped hexagonal array pin bundles," *Nuclear Engineering and Design,* vol. 267, no. 1, pp. 109-131, 2014.

[35] E. Merzari, "High fidelity cfd simulation of wire-wrapped 61-pin bundle with nek5000," in *ANS Winter Meeting*, 2016.

[36] J. T. Han, "Blockages in LMFBR fuel assemblies: a review of experimental and theoretical studies.," Oak Ridge National Lab, Oak Ridge TN (USA), 1977.

[37] J. Pacio, M. Daubner, F. Fellmoser, K. Liftin and T. Wetzel, "Heat transfer experiment in a partially (internally) blocked 19-rod bundlewith wire spacers cooled by LBE," *Nuclear Engineering and Design*, pp. 225-240, 2018.

[38] M. Piro, F. Wassermann, S. Grundmann, B. Leitch and C. Tropea, "Progress in on-going experimental and computational fluid dynamic investigations within a

CANDU fuel channel," *Nuclear Engineering and Design,* vol. 299, no. 1, pp. 184-200, 2016.

[39] I. Di Piazza, F. Magugliani, M. Tarantino and A. Alemberti, "A cfd analysis of flow blockage phenomena in alfred lfr demo fuel assembly.," *Nuclear Engineering and Design,* vol. 276, no. 1, pp. 202-215, 2014.

[40] H. Y. Jeong, K. S. Ha, W. P. Chang, Y. M. Kwon and Y. B. Lee, "Modeling of flow blockage in a liquid metal-cooled reactor subassembly with a subchannel analysis code," *Nuclear Technology,* vol. 149, no. 1, pp. 71-87, 2005.

[41] X. Chai, X. Liu, J. Xiong and X. Cheng, "CFD analysis offlow blockage phenomena in a LBE-cooled 19-pin wire-wrapped rod bundle," *Nuclear Engineering and Design,* vol. 344, no. 1, pp. 107-121, 2019.

[42] T. D. Nguyen, L. L. A. White, R. Vaghetto and Y. A. Hassan, "Turbulent flow and vortex characteristics in a blocked subchannel," *Experiments in Fluids,* vol. 60, no. 8, p. 129, 2019.

[43] T. D. Nguyen, L. L. A. White, R. Vaghetto and Y. A. Hassan, "High-fidelity velocity measurements in a totally blocked interior subchannel," *Nuclear Engineering and Design,* vol. 353, p. 110234, 2019.

[44] D. T. Nguyen, R. Muyshondt, Y. A. Hassan and N. K. Anand, "Experimental investigation of cross flow mixing in a randomly packed bed and streamwise vortex characteristics using particle image velocimetry and proper orthogonal decomposition analysis," *Physics of Fluids,* vol. 31, no. 2, p. 025101, 2019.

[45] T. Nguyen, N. Goth, P. Jones, S. Lee, R. Vaghetto and Y. Hassan, "PIV measurements of turbulent flows in a 61-pin wire-wrapped hexagonal fuel bundle," *International Joural of Head and Fluid Flow,* vol. 65, no. 1, pp. 47-59, 2017.

[46] LaVision, *3d calibration plates for strainmaster systems,* LaVision, 2016.

[47] A. C. Eckstein, J. Charonko and P. Vlachos, "Phase correlation processing for DPIV measurements," *Experiments in Fluids,* vol. 45, no. 3, pp. 485-500, 2008.

[48] Y. Hassan and T. Blanchet, "Flow velocity measurements using digital pulsed laser velocimetry," *Optical Engineering,* vol. 30, no. 8, pp. 1220-1228, 1991.

[49] Y. Hassan and O. G. Phillip, "A new artificial neural netwokr tracking technique for particle image velocimetry," *Experiments in Fluids,* vol. 23, no. 2, pp. 145-154, 1997.

[50] M. Raffel, C. Willert, F. Scarano, K. Fulvio, J. Christian, S. Wereley and J. Kompenhans, Particle Image Velocimetry: A Pratical Guide, Springer, 2018.

[51] J. Westerweel, "Efficient detection of spurious vectors in particle image velocimetry data," *Experiments in Fluids,* vol. 16, no. 3-4, pp. 236-247, 1994.

[52] J. Westerweel, D. Dabiri and M. Gharib, "The effect of a discrete window offset on the accurasy of cross-correlation analysis of digital piv recordings," *Experiments in fluids,* vol. 23, no. 1, pp. 20-28, 1997.

[53] A. Sciacchitano and B. Wieneke, "PIV uncertainty propogation," *Measurement Science and Technology,* vol. 27, no. 8, p. 084006, 2016.

[54] A. Sciacchitano, D. R. Neal, B. L. Smith, S. O. Warner, P. P. Vlachos, B. Wieneke and F. Scarano, "Collaborative framework for PIV uncertainty quantificcation: comparative assessment of methods," *Measurement Science and Technology,* vol. 26, no. 7, p. 074004, 2015.